146 (2023) 213289

Contents lists available at ScienceDirect

Biomaterials Advances

journal homepage: www.journals.elsevier.com/materials-science-and-engineering-c

Tumor decellularization reveals proteomic and mechanical characteristics of the extracellular matrix of primary liver cancer

Gilles S. van Tienderen [a], James Conboy [b], Iain Muntz [b], Jorke Willemse [a], Jantine Tieleman [c], Kathryn Monfils [a], Ivo J. Schurink [a], Jeroen A.A. Demmers [c], Michail Doukas [d], Gijsje H. Koenderink [b], Luc J.W. van der Laan [a], Monique M.A. Verstegen [a,*]

[a] Department of Surgery, Erasmus MC Transplant Institute, University Medical Center Rotterdam, Rotterdam, the Netherlands
[b] Department of Bionanoscience, Kavli Institute of Nanoscience Delft, Delft University of Technology, Delft, the Netherlands
[c] Proteomics Center, Erasmus University Medical Center, Rotterdam, the Netherlands
[d] Department of Pathology, Erasmus MC – University Medical Center, Rotterdam, the Netherlands

ARTICLE INFO

Keywords:
Decellularization
Extracellular matrix
Primary liver cancer
Hepatocellular carcinoma
Cholangiocarcinoma

ABSTRACT

Tumor initiation and progression are critically dependent on interaction of cancer cells with their cellular and extracellular microenvironment. Alterations in the composition, integrity, and mechanical properties of the extracellular matrix (ECM) dictate tumor processes including cell proliferation, migration, and invasion. Also in primary liver cancer, consisting of hepatocellular carcinoma (HCC) and cholangiocarcinoma (CCA), the dysregulation of the extracellular environment by liver fibrosis and tumor desmoplasia is pertinent. Yet, the exact changes occurring in liver cancer ECM remain uncharacterized and underlying tumor-promoting mechanisms remain largely unknown. Herein, an integrative molecular and mechanical approach is used to extensively characterize the ECM of HCC and CCA tumors by utilizing an optimized decellularization technique. We identified a myriad of proteins in both tumor and adjacent liver tissue, uncovering distinct malignancy-related ECM signatures. The resolution of this approach unveiled additional ECM-related proteins compared to large liver cancer transcriptomic datasets. The differences in ECM protein composition resulted in divergent mechanical properties on a macro- and micro-scale that are tumor-type specific. Furthermore, the decellularized tumor ECM was employed to create a tumor-specific hydrogel that supports patient-derived tumor organoids, which provides a new avenue for personalized medicine applications. Taken together, this study contributes to a better understanding of alterations to composition, stiffness, and collagen alignment of the tumor ECM that occur during liver cancer development.

1. Introduction

The extracellular matrix (ECM) is a highly organized complex ensemble of cross-linked structural proteins and associated (growth) factors which together form a dynamically regulated tissue environment. Dysregulations of ECM dynamics occur during tumor progression. Many tumors are associated with a distinct ECM signature, e.g. ECM stiffening and collagen fiber alignment, directing aspects of tumor behavior [1,2]. Biochemical and biophysical cues from the ECM are crucial in instructing cell phenotype and tissue architecture in both healthy and diseased tissue. Understanding the complexity of ECM in diseased tissue, both on a mechanical and biochemical level, could provide important context for understanding disease progression, identifying potential biomarkers, and allowing for improved in vitro

Abbreviations: ECM, extracellular matrix; PLC, primary liver cancer; HCC, hepatocellular carcinoma; CCA, cholangiocarcinoma; PSR, PicroSirius red; DAPI, 4′,6-diamidino-2-phenylindole; PI, propidium iodide; sGAG, sulfated glycosaminoglycans; SHG, second harmonic generation; BME, basement membrane extract; TECM, tumor extracellular matrix hydrogel; ECM-2, extracellular matrix protein 2; MATN3, matrilin 3; KITLG, KIT ligand; PPBP, pro-platelet basic protein; RSPO3, R-spondin 3; WNT2, Wnt family member 2; COCH, cochlin; BMPER, BMP binding endothelial regulator; LUM, lumican; POSTN, periostin; OGN, osteoglycin; PODN, podocan; SERPINA10/B5//D1/E1, serpin family A/B/D/E member 10/5/1/1; PFA, paraformaldehyde; DE, differentially expressed; LAMA1, laminin subunit alpha 1; MUC5B, mucin 5B.

* Corresponding author at: Dr. Molewaterplein 40, Room Na1005, 3015 GD Rotterdam, the Netherlands.
E-mail address: m.verstegen@erasmusmc.nl (M.M.A. Verstegen).

https://doi.org/10.1016/j.bioadv.2023.213289
Received 17 October 2022; Received in revised form 9 January 2023; Accepted 10 January 2023
Available online 18 January 2023

tumor tissue engineering through mimicking a more in vivo-like environment [3,4]. Current approaches in tissue engineering aim to faithfully recapitulate the ECM scaffolding and signaling, but only recently have studies been focused on comprehensively identifying the composition and biomechanics of native ECM [5–9]. Thus, in-depth studies on the global protein constituents of cancer ECM and the associated changes in network architecture and mechanics occurring during cancer progression are crucial [10].

In primary liver cancer (PLC), primarily being hepatocellular carcinoma (HCC) and cholangiocarcinoma (CCA), ECM dysregulation plays a prominent role in multiple facets of tumor behavior, including initiation and progression [11,12]. HCC often develops in already damaged environments containing large areas of inflammation and fibrosis, while CCA is commonly characterized by significant desmoplasia, meaning the extensive formation of connective tissue surrounding the tumor [13,14]. In addition, PLC is characterized by unique histological features, a widely variable mutational landscape, and high etiological and biological heterogeneity [15,16]. This highly diverse behavior of PLC is a consequence of the complex interactions between malignant cells and their microenvironment. The result is a malignancy with dismal prognosis, being the third leading cause of cancer mortality worldwide [17,18]. Uncovering the role of the extracellular environment in PLC is important to increase understanding of tumor behavior.

Interestingly, decellularization techniques provide the possibility of isolating native, human ECM with preserved tissue architecture. These methods have been widely used in tissue engineering approaches [19–24]. The ECM of the non-cancerous liver has been studied previously, which has identified important components for healthy liver tissue engineering applications [25]. However, applications of tissue decellularization within liver cancer research are lacking, particularly focused on integrating biomechanical and biochemical data.

Herein, we present the decellularization of liver tumors and adjacent liver tissues and extensively characterize the biochemical/proteomic and biomechanical properties of the resulting decellularized scaffolds. Integrating biomechanical characteristics, both on a macro and micro-scale, with protein composition data provides a global overview of the changes occurring in the ECM after development of HCC and CCA. Additionally, to showcase the use of decellularized matrix for tumor tissue engineering applications, a tumor-derived hydrogel was made that supports the culture of patient-derived tumor organoids.

2. Results

2.1. Decellularization of liver cancer tissue for isolation of extracellular matrix scaffolds

Tissue specimens from both liver cancer and adjacent tumor-free liver tissue were obtained through surgical resection or transplantation procedures (Table S1). Decellularization of small tumor and adjacent biopsies was optimized in regards to method and duration (Fig. 1A, Fig. S1). To confirm the retention of the extracellular matrix (ECM) after decellularization, histological sections were stained with hematoxylin & eosin (H&E) (Fig. 1B). The organotypic and tumor-specific morphology of the ECM remained unchanged upon decellularization. For example, decellularized CCA tissue displayed a characteristic dense ECM surrounding the tumor cells, which was retained after decellularization, while this phenomenon was absent in CCA adjacent ("-ADJ") tissue. DAPI staining confirmed successful removal of cell nuclei and DNA remnants (Fig. 1C). Quantitative analysis of DNA content confirmed successful decellularization of CCA, CCA-ADJ, HCC, and HCC-ADJ tissue through a decrease in DNA content in all biological replicates, equaling an average reduction by 97.7 %, 98.9 %, 99.1 %, and 98.6 %, respectively (Fig. 1D). These values adhere to the well-known criteria for decellularization of $<$50 ng DNA/mg wet tissue [19]. Quantitative analysis of collagen showed a high level of retention in all conditions, ranging from a 1.9 to 5.2$\times$ increase in relative concentration compared to the original tissue (Fig. 1E). To note, the apparent increase in amount of collagen that is present after decellularization, is primarily due to removing the (weight of the) cells, thus shifting the total relative concentration. Sulfated glycosaminoglycans (sGAG), which are important regulators of tumor processes such as angiogenesis, invasion, and metastasis [26,27], are also retained after decellularization, although with a lower concentration ranging from 0.34$\times$ to 0.60$\times$ compared to the original tissue (similar to collagen, the removal of cellular weight influences the relative concentration). Consolidating these findings, the ratio of sGAG to collagen showed significant differences between conditions, particularly in case of HCC, and this difference was maintained after decellularization (Fig. S2). This suggests maintenance of tumor-specific sGAGs, particularly considering that PLC is related to changes in composition of sGAGs [28,29]. In summary, decellularization of liver cancer biopsies resulted in the successful production of acellular scaffolds, which preserve relevant components of the ECM.

2.2. Proteomic characterization of decellularized scaffolds reveals diverse abundance of ECM-related proteins

To get a deeper understanding of the ECM proteins that are present in the tumor and tumor-free adjacent liver scaffolds, mass spectrometry based proteomics was employed (Fig. 2A). Subsequently, proteins were sub-divided into categories according to matrisome classification standards [8,30]. This classification divides proteins into core matrisome or matrisome-associated. The core matrisome forms the architecture of the ECM and comprises of collagens (this includes trans-membrane collagen types), ECM glycoproteins (i.e. fibronectins, laminins, tenascins, fibrillins, etc.), and proteoglycans. The matrisome-associated proteins can also be further divided into ECM-affiliated proteins (proteins structurally related to the ECM such as mucins, lectins, and syndecans), ECM regulators (this encompasses cross-linkers, modifying enzymes, proteases and protease inhibitors), and secreted factors (secreted proteins that can bind to the ECM, most commonly growth factors such as TGF-beta, BMP, Wnt). This classification is not infallible, e.g. secreted factors also includes growth factors that are currently not proven to be associated with ECM, but it does provide a framework for further modifications based on future findings [8]. Proteomic analysis of decellularized CCA and HCC led to the detection and identification of numerous unique proteins, including core matrisome and more lowly-abundant matrisome-associated proteins. In particular, core constituents of the matrisome, collagens and glycoproteins, were well-represented in both the number of unique proteins and their abundances, which are based on the summed tryptic peptide intensities (Fig. 2B, Fig. S3). However, matrisome-associated components were also detected, albeit with lower abundance, showing the suitability of the employed method to detect a wide range of ECM-related proteins (Fig. 2C, Fig. S3).

To validate our dataset, a comparison was made to proteins that have been found upregulated in liver tissue according to the human protein atlas [31]. This showed extensive overlap with highly abundant proteins identified in the decellularized samples (Fig. S4), which demonstrates the capability of the mass spectrometry preparation methods in combination with decellularization in retaining the complex assembly of extracellular matrix proteins. This deep proteomic coverage may provide better understanding of lesser represented but important components of the human liver cancer matrisome. We further validated this dataset through comparison with a previously published healthy liver matrisome profile in which 140 native human liver matrisome proteins were identified [25]. Of these 140 proteins, 96.4 % overlapped with our dataset, with only 5 proteins (COL17A1, LAMA1, PALPN, LGSALS9B, MUC5B) absent in our samples (Supplementary File 1). Importantly, we identified an additional 70 proteins that were present in all conditions and all biological replicates, thus adding to the overall knowledge on the global liver (cancer) matrisome profile (Fig. 2D). Next, we sought to determine the differences between tumor and adjacent ECM

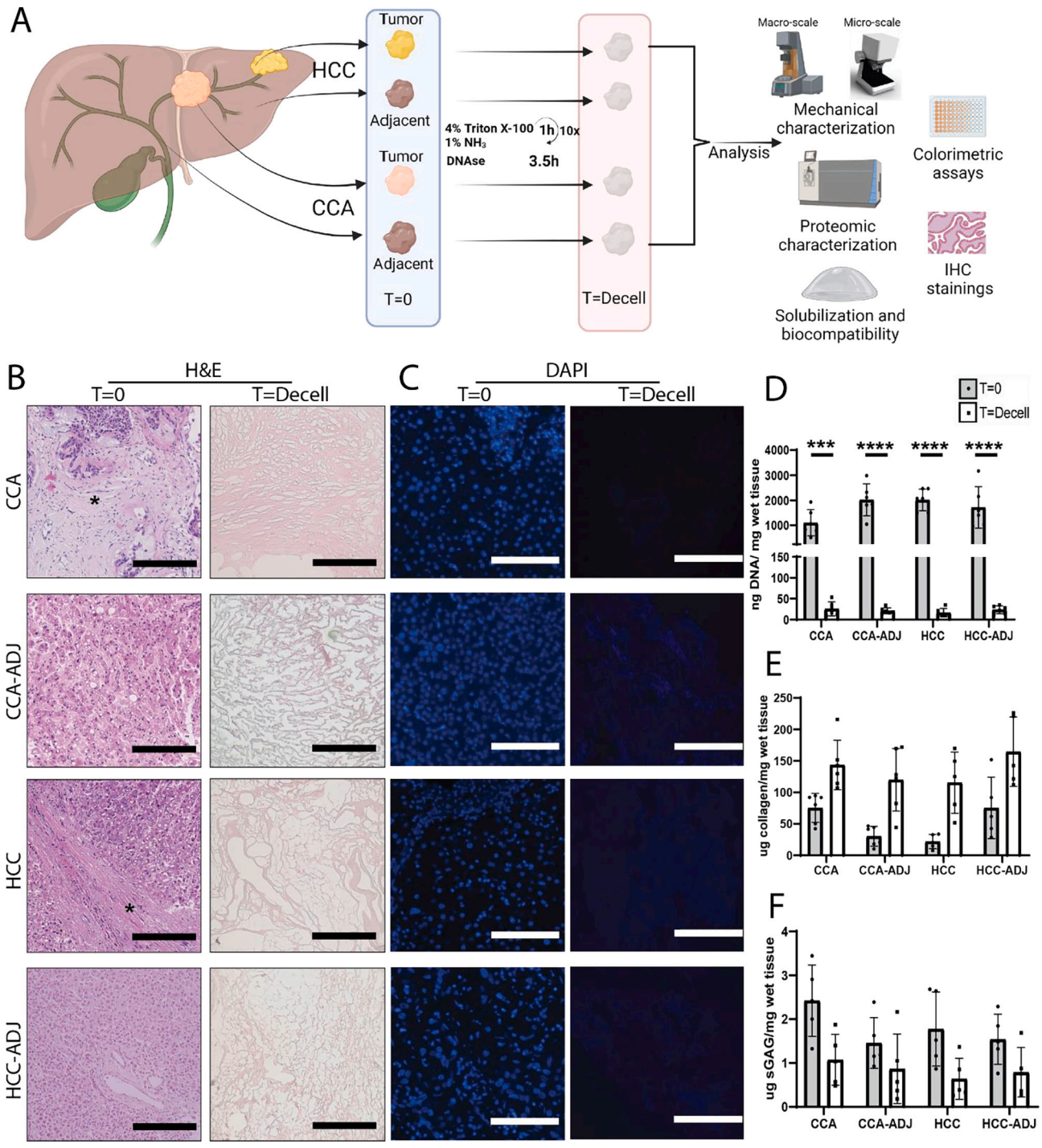

Fig. 1. Extracellular matrix obtained by decellularization of primary liver cancer tumor and adjacent liver tissue.
A) Schematic representation of the decellularization procedure and analysis of the obtained isolated extracellular matrix (ECM).
B) Representative hematoxylin & eosin stainings of tumor and adjacent tissue before (T = 0) and after (T = Decell) decellularization indicates removal of cell nuclei and maintenance of ECM structure. Scale bar indicates 200 μm. * Indicates dysplastic/fibrotic areas as determined by pathological assessment.
C) DAPI staining of tumor and adjacent tissue before and after decellularization shows absence of nuclear material in all decellularized tissues. The faintly visible blue color in all decellularization conditions is derived from the auto fluorescence of the tissues. Scale bar indicates 100 μm.
D) Quantitative DNA content analysis of tissue before and after decellularization shows a significant decrease in DNA content in all conditions present (N = 6 per condition), confirming successful decellularization.
E) Total collagen content before and after decellularization, showing a clear retention of collagen in all samples (N = 5 per condition) after decellularization.
F) Sulfated glycosaminoglycan (sGAG) content before and after decellularization, showing retention in all samples (N = 5 per condition) though with an overall decrease compared to the original tissue. A two-way ANOVA with Sidak's multiple comparisons test was used for statistical analysis of DNA content. * indicates p-value < 0.05, ** indicates p-value < 0.01, *** indicates p-value < 0.001, **** indicates p-value < 0.0001.

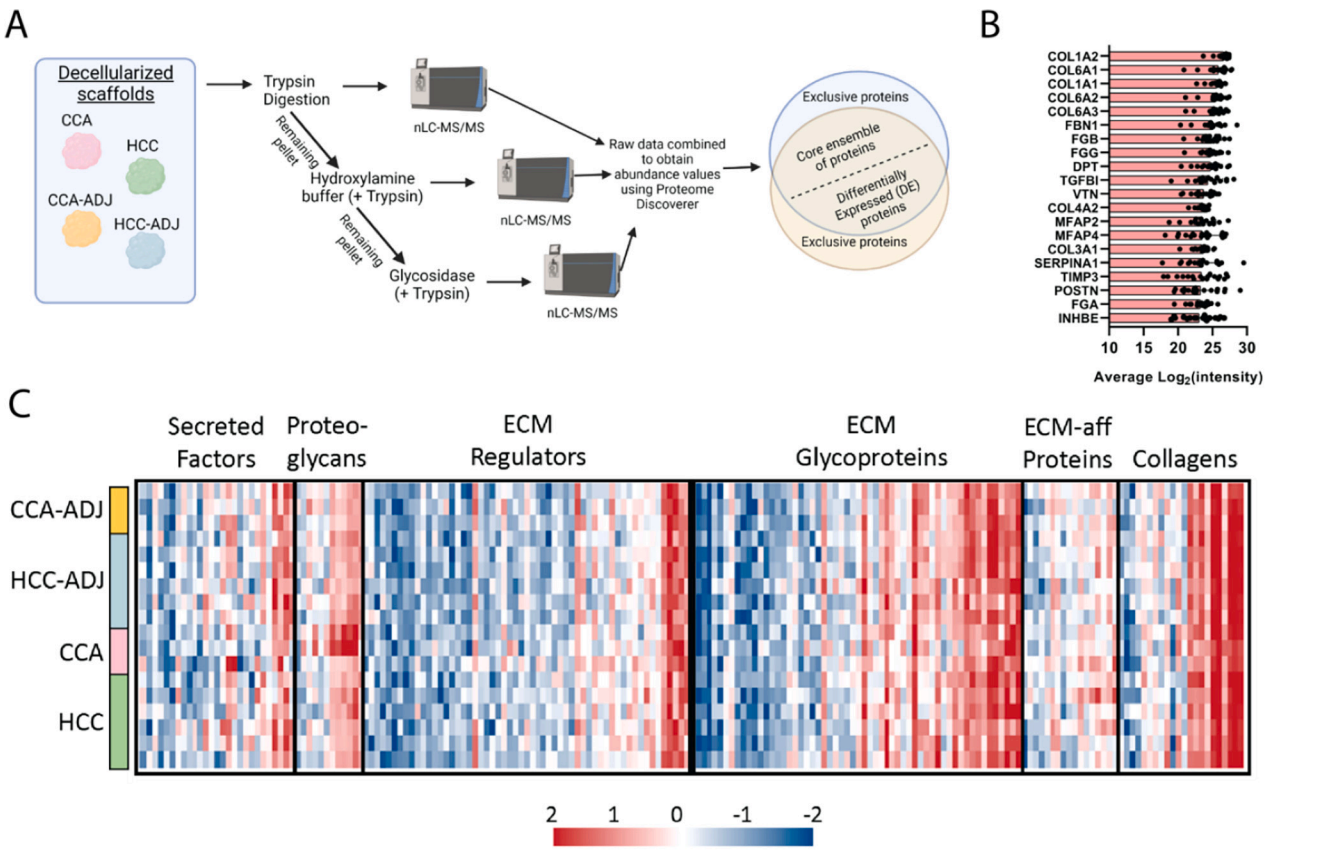

D

Core Matrisome

Collagens		Glycoproteins					Proteoglycans
COL1A1	COL6A6	AEBP1	FBLN2	LAMA4	MFAP4	TGFBI	ASPN
COL1A2	COL8A1	AGRN	FBLN5	LAMA5	MFAP5	THBS1	BGN
COL3A1	COL8A2	COMP	FBN1	LAMB1	MFGE8	THBS2	DCN
COL4A1	COL10A1	DPT	FBN3	LAMB2	MGP	THSD4	FMOD
COL4A2	COL11A1	ECM1	FGA	LAMB3	MXRA5	TINAGL1	HSPG2
COL4A3	COL12A1	EFEMP1	FGB	LAMC1	NID1	TNC	LUM
COL5A1	COL14A1	EFEMP2	FGG	LGI4	NID2	TNXB	OGN
COL5A2	COL16A1	ELN	FN1	LTBP1	NPNT	VTN	PRELP
COL5A3	COL18A1	EMID1	HMCN1	LTBP2	POSTN	VWA1	PRG2
COL6A1	COL21A1	EMILIN1	HMCN2	LTBP3	PXDN	VWF	PRG3
COL6A2		EMILIN2	IGFALS	LTBP4	SRPX		PRG4
COL6A3		FBLN1	IGFBP3	MFAP2	SRPX2		VCAN

Matrisome-associated

ECM-aff Proteins		ECM Regulators					Secreted Factors		
ANXA1	HPX	A2M	CTSD	ITIH4	PLG	SERPINF1	ANGPTL2	MST1	WNT4
ANXA11	LGALS1	ADAMTS13	CTSF	ITIH5	PLOD1	SERPINF2	ANGPTL6	PDGFD	WNT6
ANXA13	LGALS3	ADAMTS4	CTSG	KNG1	PRSS1	SERPING1	CCL19	S100A11	WNT9B
ANXA2	LGALS4	ADAMTS5	ELANE	LOX	SERPINA1	SERPINH1	CXCL12	S100A12	
ANXA3	SEMA3B	ADAMTSL4	F13A1	LOXL1	SERPINA10	SLPI	CXCL13	S100A4	
ANXA4		AGT	F9	MMP11	SERPINA3	TGM2	EBI3	S100A7	
ANXA5		AMBP	HRG	MMP12	SERPINA4	TGM3	EGFL7	S100A8	
ANXA6		BMP1	HTRA1	MMP14	SERPINA5	TIMP1	FGF23	S100A9	
ANXA7		C17orf58	HTRA3	MMP19	SERPINB1	TIMP3	INHBB	S100P	
C1QB		CTSA	ITIH1	MMP23B	SERPINC1		INHBC	TGFB1	
C1QC		CTSB	ITIH2	MMP28	SERPIND1		INHBE	TNFSF13	
CLEC11A		CTSC	ITIH3	MMP7	SERPINE2		MEGF6	WNT11	

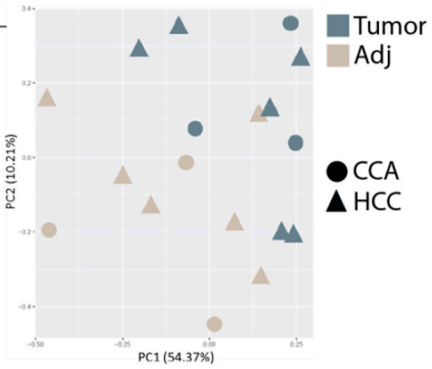

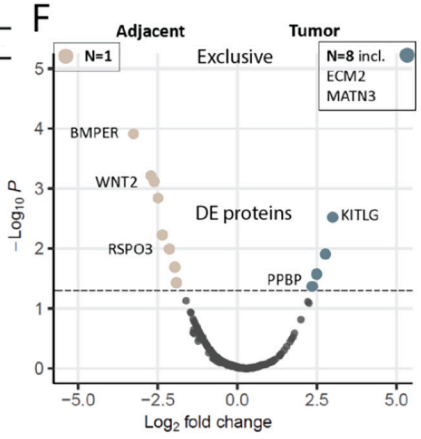

(caption on next page)

Fig. 2. Analysis of ECM proteome derived from decellularized liver tumor and adjacent tissue.
A) Schematic overview of the procedure used for the identification of ECM proteins with mass spectrometry. Three different variants of trypsin digestion were used to extract the proteins from the decellularized scaffolds. Proteins were included in the core ensemble if no significant difference was observed between conditions, and identified as DE if there was a significant difference (adj. p-value < 0.05). If a protein was present in the samples of one condition and absent in all samples of another condition it was classified as exclusive.
B) Average intensity of the top 20 most abundant ECM-related proteins. The most abundant proteins primarily consist of collagens. Black dots represent individual data points ($N = 18$).
C) Heatmap visualizing the relative abundance (z-score, color bar) of different ECM proteins in each sample (CCA, HCC, CCA-ADJ, HCC-ADJ) highlighting the diversity of proteins identified. A multitude of proteins were observed in all categories, with relative high global similarity between samples.
D) Ensemble of ECM-related proteins present in all samples, separated based on sub-categories as defined by MatrisomeDB. Only proteins that are present in all replicates ($N = 18$) are included in the ensemble.
E) Scatter plot based on principal component analysis (PCA) displays a global separation between tumor and adjacent ECM samples in regards to ECM protein abundance. A division between tumor and adjacent ECM can be seen, with one cirrhotic HCC-ADJ sample clustering within the tumor samples as an exception.
F) Volcano plot containing differentially expressed (DE) proteins and exclusively identified proteins comparing tumor (HCC and CCA combined, $N = 9$) and adjacent tissue ($N = 9$). The top left and right dots represent the exclusively identified proteins in either setting, with the number representing the amount of different proteins identified. Differential expression was defined as an adjusted p-value of <0.05.

composition. Globally, Principal Component Analysis revealed differences in protein abundance through a division between HCC and CCA tumor and adjacent samples, with the exception of a cirrhotic HCC-ADJ scaffold (Fig. 2E).

To dive further into the differences between tumor and adjacent matrisome profiles, protein expression was analyzed through differential expression (DE) and identification of exclusive proteins. We identified a multitude of matrisome-related proteins that are affected by the development of liver cancer (Supplementary File 2). In total, comparing liver tumor ($N = 9$) and adjacent decellularized ECM ($N = 9$), we found 21 differences in protein abundance (Fig. 2F). Amongst these, ECM protein 2 (ECM2), which is a regulator of assembly and deposition of ECM [32], is overexpressed in tumor and was previously identified as a tumor progression marker in HCC [33]. Other proteins, such as MATN3, KITLG, and PPBP have previously been reported to be overexpressed in other tumors [34–37]. These findings suggest that MATN3, KITKG, and PPBP might play a role in PLC as well. In contrast, RSPO3 was found to be significantly enriched in adjacent decellularized liver tissue and previously found to be significantly decreased in prostate cancer [38]. Furthermore, together with the overabundance of WNT2 in adjacent tissue, this hints at the importance of the Wnt pathway in maintaining a non-tumor environment. This coincides with the notion that dysregulation of Wnt signaling leads to the development of various cancers [39,40].

2.3. Tumor-specific ECM remodeling for HCC and CCA

To address potential tumor-specific differences, patient-paired analysis of tumor and adjacent ECM was performed for both HCC and CCA. Significant differences in ECM-related compositional changes were found when comparing CCA and HCC to their respective adjacent ECM (Fig. 3A, B), as well as when comparing CCA to HCC tumor ECM (Fig. 3C). Overlap with the global tumor scaffold matrisome profile (Fig. 2F) was found for both tumor types, but CCA had an additional 22/33 (66.7 %) ECM proteins that are significantly changed, compared to 16/27 (59.3 %) for HCC. The largest number of differences were found when comparing tumor-types (total 52 proteins). The comparison between HCC and CCA tumor tissue is not a patient-paired analysis, thus automatically containing more patient-to-patient heterogeneity within the samples. To note, serpins (mostly SERPINB5, SERPINE1, SERPIND1, SERPINA10), a superfamily of proteins with multiple roles in cancer, particularly related to proteolysis [41], are prominently affected when comparing CCA and HCC ECM. This suggests a tumor-type specific role for these proteases in the development of liver cancer.

To evaluate further whether this approach adds novel insights into liver cancer biology, we integrated and compared the data with publically available TCGA RNA sequencing datasets for CCA, HCC, and adjacent tissues (see Methods). Each comparison displayed some level of overlap with DE genes from the RNA sequencing datasets (CCA vs CCA-ADJ 58.8 %, HCC vs HCC-ADJ 84.4 %, HCC vs CCA 53.8 %) (Fig. 3D–F, Supplementary File 3). On top of that, 43 additional proteins were discovered to be differentially regulated in the context of HCC and CCA. This shows the increased sensitivity of decellularization combined with protein level analysis compared to large RNA sequencing datasets to discover changes in ECM-related proteins. Elaborating on this, enrichment analysis was performed to relate changes found in the identified proteins to the expression of functionally related pathways (Fig. 3G–I, Supplementary File 4). Specifically, comparison of CCA and CCA-ADJ showed that CCA had an increased abundance of ECM regulators, while the adjacent ECM contained more secreted factors (Fig. 3G). Interestingly, proteins associated with collagen fibril organization, known to play a vital role in metastasis and clinical outcome in multiple cancer types, were enriched in CCA [42]. This indicates that fibrillary organization is a focal point of tumor ECM remodeling, rather than purely changes in collagen composition. This is also highlighted by the absence of significant differences in collagen abundance (Fig. S5). Comparing HCC to HCC-ADJ resulted in less distinct features as seen by limited enrichment of functional pathways (Fig. 3H). Additionally, comparing HCC and CCA unveiled an important role for proteolysis regulation in CCA, relating back to the large amount of serpins significantly enriched (Fig. 3C, I). Furthermore, the expression levels amongst all the different conditions (CCA, CCA-ADJ, HCC, HCC-ADJ) were compared to select individual ECM proteins that exhibited high abundance or that showed significant changes in expression (Fig. 3J). This analysis revealed four primary expression patterns. A total of 8 ECM-related proteins are differentially expressed regardless of tumor type (e.g. COCH, ECM2, BMPER), while 44 proteins exhibit tumor-type-specific expression patterns compared to the adjacent ECM (e.g. LUM, POSTN, CSTB, MMP9). Moreover, 26 proteins showed a change in expression only when comparing the two tumor-types (e.g. COL5A3, MMP7, OGN). A multitude of proteins, containing an over-representation of collagens, showed similar abundance across all conditions (e.g. COL1A1, COL3A1, PODN, COL15A1). The complete protein list can be found in Supplementary File 3. In all, these data suggest that the global structure as defined by specific collagens present is not heavily affected during tumor progression in the liver, regardless of tumor type. Rather, the matrisome-associated proteins of the extracellular matrix play a vital role in the remodeling of ECM composition during the development of liver cancer.

2.4. Decellularization preserves tumor-specific differences in collagen composition

To confirm the trends in core ECM protein expression, immunostainings were performed to visualize the global collagen presence. PicroSirius Red (PSR) staining confirmed and validated the global abundance of collagens in all groups, which is clearly retained and preserved after decellularization (Figs. 2B, 4A, B). Furthermore, an

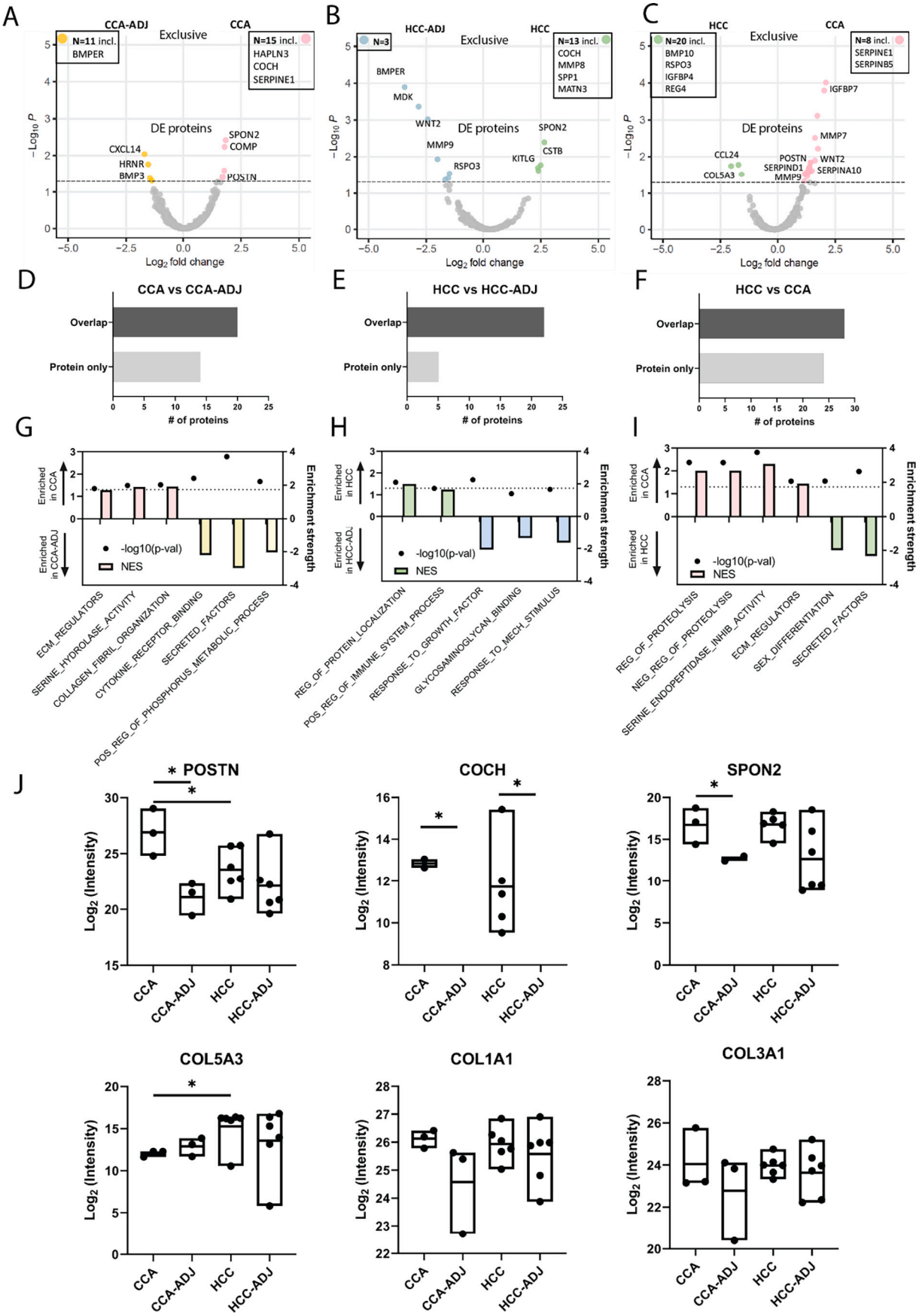

(caption on next page)

Fig. 3. Tumor-specific differences in ECM proteome and associated pathways.
A, B, C) Volcano plot containing differentially expressed (DE) proteins and exclusively identified proteins comparing (A) CCA-ADJ and CCA, (B) HCC-ADJ and HCC, and (C) HCC and CCA. The top left and right dot represent the exclusively identified proteins in either setting, with the number representing the amount of different proteins identified.
D, E, F) Bar chart displaying unique DE proteins only detected by decellularization proteomics (proteome only) versus DE genes detected both on RNA and protein level (both transcriptome and proteome). The DE genes were obtained from public bulk RNA sequencing datasets and DE proteins as determined via mass spectrometry of our decellularized samples for (D) CCA and CCA-ADJ, (E) HCC and HCC-ADJ, (F) HCC and CCA. See File S3 for all DE genes identified in the RNA sequencing datasets.
G, H, I) Enrichment analysis of selected biological processes and pathways for protein abundance differences (exclusive + DE) comparing (G) CCA and CCA-ADJ, (H) HCC and HCC-ADJ, (I) HCC and CCA.
J) Box plots showing abundance levels of proteins representative for the four main groups of expression patterns found when comparing the different decellularized scaffolds. Black dots represent individual data points. All box plots indicate mean (center line) and min and max value (bound of box). Significance level is marked with an asterisk (* = p value < 0.05).

increase in total PSR staining in CCA compared to CCA-ADJ is visible (Fig. 4A). Similar results are found when comparing total collagen intensity by mass spectrometry, with a 2.0× higher total collagen intensity in the combined abundance of collagens in CCA compared to CCA-ADJ, while HCC only showed a 1.2× higher total collagen intensity compared to HCC-ADJ. Collagen type 1 is highly expressed in all conditions (Fig. 4B, Fig. S6A), with more diffuse expression of collagen type 3 (Fig. 4C). No clear qualitative differences in relative amounts are visible, validating the mass spectrometry results. It is well known that tumor progression is often accompanied by collagen fiber reorganization [43,44]. To visualize the overall structure of collagen fibers, Second Harmonic Generation (SHG) was used (Fig. 4D). Through application of software packages CT Fire and CurveAlign fiber length and collagen alignment could be measured, respectively [45,46] (Fig. S7). In both tumor types the length of collagen fibers was significantly longer compared to their adjacent counterparts (mean ± SEM CCA vs CCA-ADJ 39.4 ± 0.32 vs 37.0 ± 0.42, $p < 0.001$, HCC vs HCC-ADJ 40.8 ± 0.42 vs 37.3 ± 0.39, $p < 0.001$, Fig. S8). Interestingly, CCA showed a significantly higher alignment coefficient compared to CCA-ADJ (mean ± SD CCA vs CCA-ADJ 0.47 ± 0.08 vs 0.33 ± 0.1, $p = 0.04$), which was not present when comparing HCC and HCC-ADJ (Fig. 4F).

2.5. Inter- and intra-tumor heterogeneity in mechanical properties of liver cancer ECM

Next, we sought to determine if the observed differences in ECM composition and collagen alignment resulted in different biomechanical properties of liver cancer decellularized scaffolds through macro- and micro-scale measurements. For this, rheology and nanoindentation were employed, respectively. Rheological properties of the decellularized scaffolds were assessed using a parallel plate geometry at various compression levels (Fig. S9). All conditions showed an increase in shear storage modulus (Fig. 5A, B) and normal stress (Fig. 5C, D) in response to increased compression, which recovered back toward the original levels after de-compression. For CCA samples, the shear storage modulus ranged from 45 Pa at zero compression to 266 Pa at 50 % compressive strain, while CCA-ADJ ranged from 4.6 to 81 Pa at the same compression levels. CCA was thus significantly stiffer than CCA-ADJ (G′ values paired at each compression level *t*-test, $t = 5.981$, $p = 0.0004$). This difference was absent when comparing HCC, ranging from 30 Pa at zero compression to 178 Pa at 50 % compressive strain, to HCC-ADJ, ranging from 34 Pa to 165 Pa at the same compression levels (paired at each compression level *t*-test, $t = 1.205$, $p = 0.26$). A similar difference was observed when comparing maximum normal stress in response to compression, with CCA being stiffer in compression than CCA-ADJ (CCA 1085 ± 1360 Pa vs CCA-ADJ 471 ± 539 Pa, $p = 0.03$) while HCC was comparable to HCC-ADJ (HCC vs HCC-ADJ 865 ± 546 Pa vs 1331 ± 518 Pa, $p = 0.4$, Fig. 5C, D). Accordingly, calculation of the Young's modulus over the range of compressive strains showed the highest stiffness in CCA (2959 Pa) compared to the other conditions (CCA-ADJ 765 Pa, HCC 478 Pa, HCC-ADJ 806 Pa) (Fig. S10). These data are congruent with in vivo data using magnetic resonance elastography for liver tumors, which showed the highest shear stiffness for CCA tissues [47]. Thus, the higher stiffness seems primarily due to the biomechanics of the extracellular matrix. As expected, a large inter and intra-patient heterogeneity was observed in all conditions (Fig. S11). This has important implications for tissue engineering strategies, commonly using a constant stiffness environment. Consistent with earlier studies [48–50], our findings show through the use of decellularization that natural biomechanical environments have regional and spatiotemporal differences in stiffness and elastic modulus, which could play an important role in cellular heterogeneity, differentiation and tumor development. From compression measurements, we also determined poroelastic features of the tissues by determining the characteristic relaxation time, representing the time it takes to reach equilibrium after compression for both shear storage modulus and normal stress values (Fig. S9D, Fig. 5A–D). A significant difference was observed in HCC vs HCC-ADJ for normal stress relaxation. This suggests the advent of HCC modulates the ECM through changes in pore size, as larger pores result in a faster relaxation time, rather than a change in shear storage modulus or normal stress.

Next, we aimed to probe the mechanical characteristics on a micro-scale, in order to integrate macro (rheology-based) and micro-scale (nanoindentation-based) data and provide a comprehensive analysis on the mechanical characteristics of liver cancer ECM. A high level of heterogeneity was observed on a micro-scale, with CCA decellularized ECM providing the highest effective Young's modulus (mean ± SD CCA: 16.5 ± 41.8 kPa, CCA-ADJ: 4.6 ± 7.3 kPa, HCC 2.6 ± 2.8 kPa, HCC-ADJ 4.3 ± 8.3 kPa, Fig. 5E). The effective Young's modulus is defined as the Young's modulus without making any assumptions regarding Poisson's ratio. Thus, on a micro-scale a similar trend persists, albeit with a different magnitude compared to rheology measurements. Furthermore, both CCA and HCC showed a high level of patient-to-patient heterogeneity in a tumor and adjacent setting (Fig. 5F, G). A heat map was plotted to showcase the spatial localization of stiffness regions within each scaffold (Fig. 5H). Distinct regions of high and low stiffness were observed, particularly in CCA. In all, both macro and micro-scale data showed that the development of CCA most affected the mechanical properties of the ECM. Combined with the mass spectrometry data, this suggests that ECM remodeling plays an important role in the development of liver cancer, particularly in CCA.

2.6. Tumor ECM-derived hydrogel formation and characterization

To provide a platform for improved tumor cell culture, in particularly to set up better in vitro models for tumor cell or organoid expansion, decellularization could be used to create a tumor-specific hydrogel. To obtain a biocompatible tumor-derived hydrogel, CCA tumor ECM (N = 3 patients) was lyophilized, grinded to powder, and subsequently digested by pepsin. This resulted in a viscous ECM suspension (Fig. 6A). Subsequently, with pH normalization to 7.5, the suspension formed a CCA tumor ECM hydrogel (TECMgel). The digestion efficiencies for the three patient-derived hydrogels were 30.5 %, 33.9 %, and 44.2 %, which is similar to previously published results for healthy liver ECM hydrogels

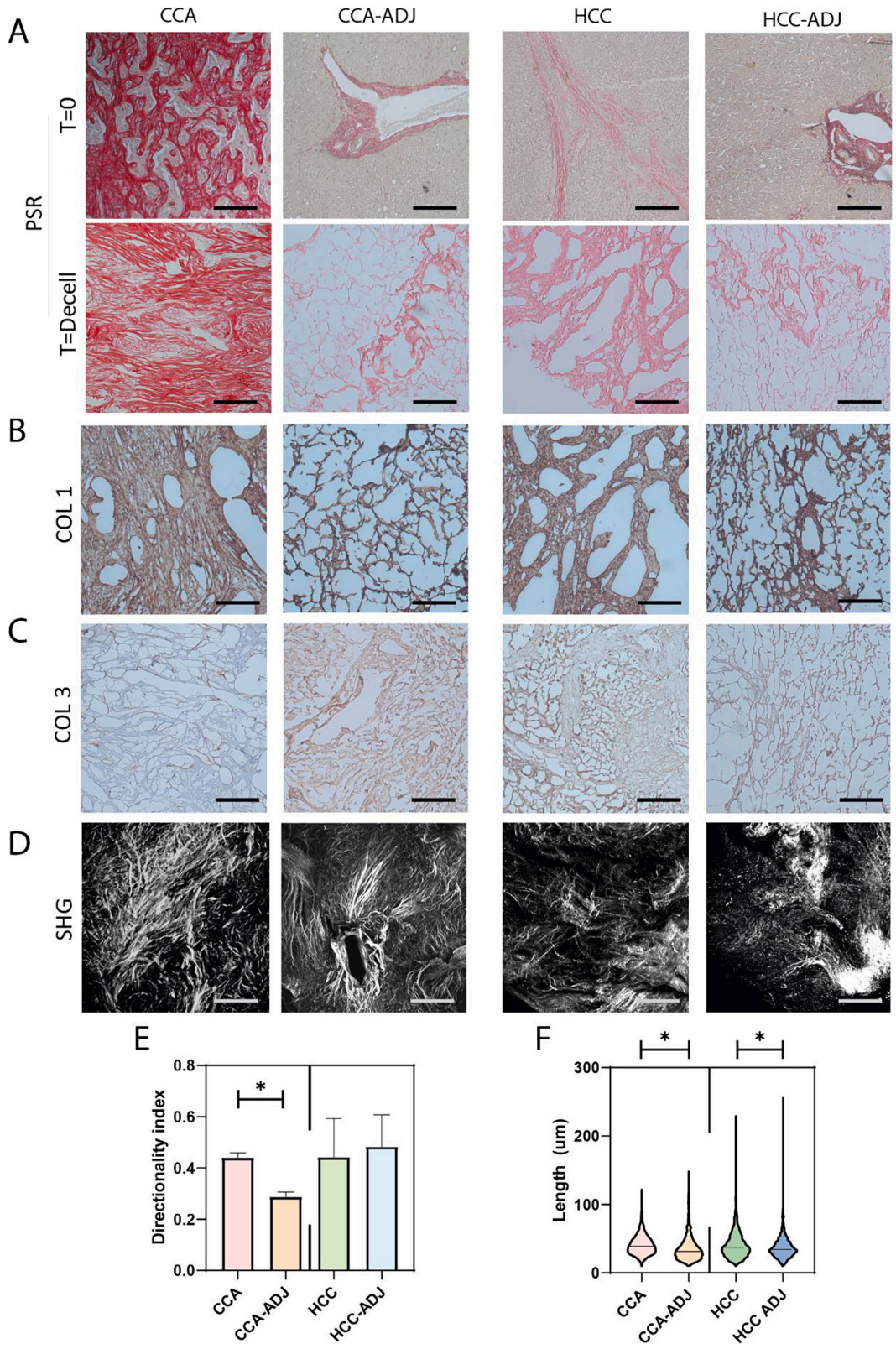

Fig. 4. Preserved topology and alignment of collagens in decellularized liver tumor scaffolds.
A, PSR staining before (T = 0) and after (T = decell) decellularization displays clear retention of collagen after the decellularization procedure in all conditions.
B, C) Collagen type 1 (C) and collagen type III (D) after decellularization shows presence and retention of both types, COL1 and COL3, of fibrillary collagen.
D) Representative second harmonic generation (SHG) confocal images of collagen fibers indicates differences in alignment patterns.
F) Histogram showing the relative alignment of collagen fibers for each sample. CCA tissue is significantly more aligned compared to its corresponding adjacent tissue. Coefficient of alignment, here represented by the directionality index, represents the range from completely isotropic (0.0) to completely aligned (1.0). The red dotted line represents the directionality index of healthy liver tissue. All scale bars indicate 250 μm. * indicates a p-value < 0.05.

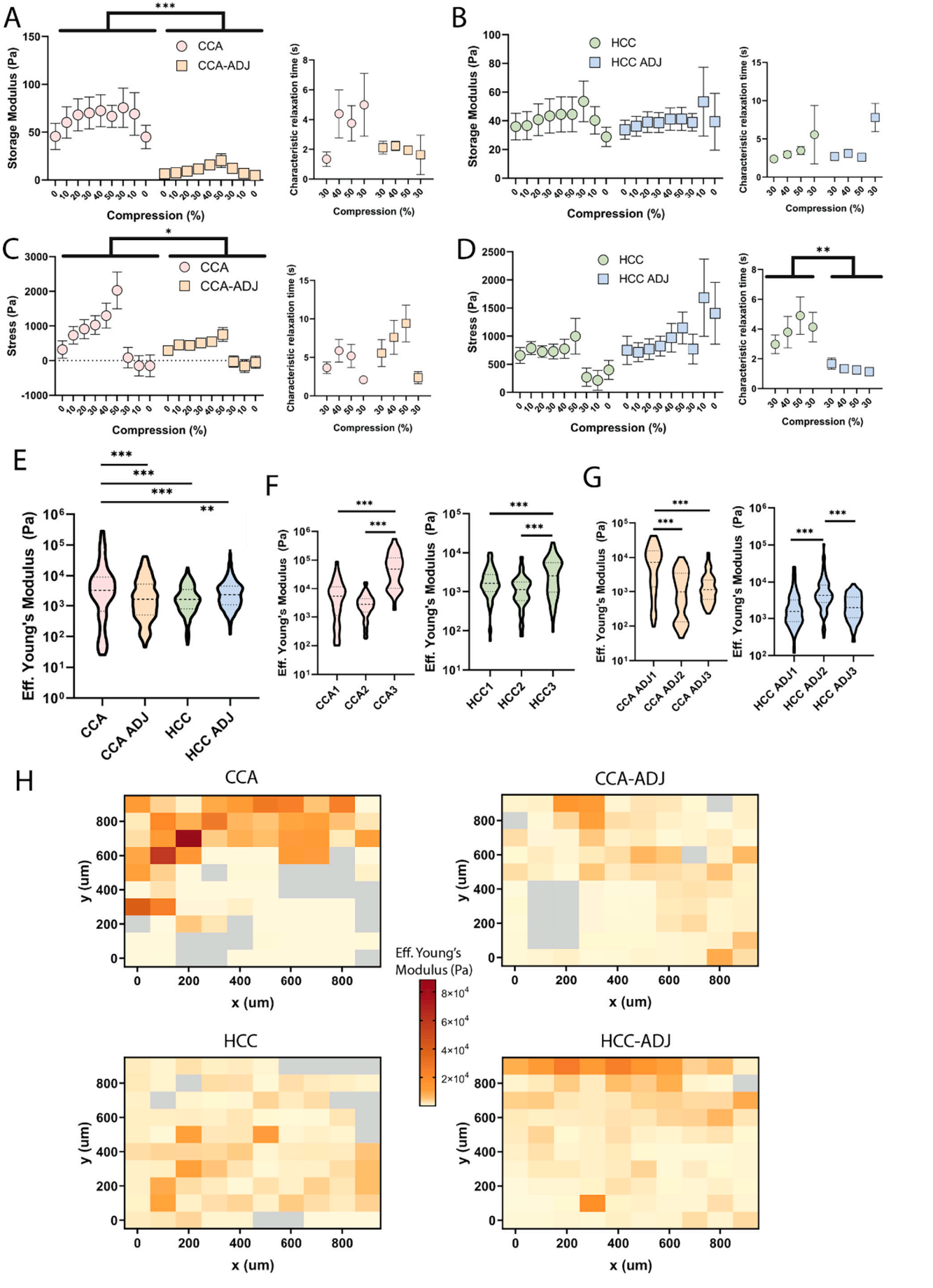

(caption on next page)

Fig. 5. Mechanical characterization of decellularized primary liver cancer scaffolds.
A, B) Rheological measurements showing storage shear modulus and characteristic relaxation time for (A) CCA vs CCA-ADJ, and (B) HCC vs HCC-ADJ at different compressive strains. CCA has a higher storage modulus compared to CCA-ADJ. A Wilcoxon paired test without assuming Gaussian distribution was used for statistical analysis.
C, D) Rheological measurements showing maximum normal stress and a characteristic relaxation time of the normal force for (C) CCA vs CCA-ADJ, and (D) HCC vs HCC-ADJ at different compression levels. HCC has a higher characteristic relaxation time compared to HCC-ADJ.
E) Violin plot visualizing the effective Young's modulus as determined by nano-indentation measurements for the different decellularized scaffolds. CCA tissue is significantly stiffer compared to CCA-ADJ, HCC, HCC-ADJ. This stiffness is heterogeneous across the tumor but stiffer than non-tumorigenic tissue.
F) Violin plot visualizing the effective Young's modulus per patient sample for CCA (top) and HCC (bottom) tumor scaffolds displaying patient heterogeneity.
G) Violin plot visualizing the effective Young's modulus per patient sample for CCA (top) and HCC (bottom) adjacent scaffolds displaying patient heterogeneity.
H) Representative heat maps of nanoindentation for CCA, CCA-ADJ, HCC, and HCC-ADJ decellularized scaffolds. Color bars represents the Young's modulus, with grey color representing values that were omitted due to having an unreliable model fit (<0.9 R^2). For all statistical analysis in this figure, * indicates p-value < 0.05, ** indicates p-value < 0.01, *** indicates p-value < 0.001.

(Fig. 6B) [51]. Analysis of sulfated glycosaminoglycan's (Fig. 6C) and collagens (Fig. 6D) showed compositional heterogeneity when comparing TECMgel-derived from different patients, congruent with the heterogeneity observed in ECM protein composition and biomechanics. This heterogeneity can be mitigated by pooling the patients' ECM hydrogels (termed 'TECMgel pool'). For the subsequent experiments, we probed the mechanical properties and cellular biocompatibility of the pooled TECMgel to provide a proof-of-concept and application of decellularized ECM. The kinetics of gelation were characterized through temperature-sweep and frequency sweep rheological experiments (Fig. 6E, Fig. S12A–C). The TECMgel showed an expected increase in storage modulus (G′) with an increase in concentration from 4 mg/ml to 6 mg/ml (Fig. S12A). The 6 mg/ml TECMgel showed a stable G′ of 337 Pa after gelation (Fig. 6E). The frequency sweep data showed a considerably higher storage than loss modulus, as expected for a primarily elastic material. Additionally, there is little frequency dependence for the storage modulus, indicating a stable gel structure formed, as expected for collagen based hydrogels (Fig. S12C). The differential modulus (K′) measured as the slope of stress/strain curves recorded in stress ramps revealed no non-linear behavior until rupture (Fig. 6F). This contrasts with the behavior of hydrogels reconstituted from purified collagen, which have previously been shown to show extensive strain stiffening [52]. The differences in K′ and G′ (Fig. 6F, E) are mainly due to the viscous dissipative deformation which we assume to be present because of the relatively large values for loss modulus. Nanoindentation showed that on a micro-scale, the TECMgel had an average effective Young's modulus of 145 Pa, which is roughly within the same order of magnitude as K′ (Fig. 6G). To note, the spatial distribution of stiffness is more homogenous in the TECMgel compared to decellularized matrix (Fig. S12D, Fig. 5H). The brittle nature of the hydrogel was confirmed by the limited recovery of G′ after the stress ramp, indicating irreversible damage (Fig. S12D).

2.7. Tumor-derived hydrogel supports culture of cell lines and patient-derived organoids

Finally, the biocompatibility of the hydrogel was extensively assessed by culturing liver cancer-related cell lines HepG2 and TFK-1 (Fig. 6H). After encapsulation, bright field images showed the formation of a densely packed cellular structure for TFK1 and HepG2, which contained mostly live cells as assessed by Calcein-AM/Propidium Iodide staining of cell-laden hydrogel structures. Furthermore, HepG2 grown in the TECMgel formed a necrotic core, similar to solid tumor behavior in vivo [53]. H&E staining confirmed the presence of tightly packed cellular structures within the TECMgel, which is clearly distinct from their 2D morphology as well as encapsulation in animal tumor-derived hydrogels such as basement membrane extract (BME) (Fig. 6H, Figs. S13, S14A). Cells that were seeded on top of the TECMgel remained alive and had different morphology when compared to conventional 2D culture without a hydrogel (Fig. S14B, C). ATP-content measurements confirmed the proliferation of HepG2 and TFK-1 cells encapsulated in TECMgel. The total ATP content increased at 7 days of culture, indicating cellular proliferation (Fig. 6I). In addition to cancer cell lines, the culture of tumor organoids in the TECMgel was also assessed. We previously initiated three patient-derived cholangiocarcinoma organoids (CCAO) and confirmed their tumorigenicity [54]. These CCAO were cultured in the TECMgel to create a fully patient-derived in vitro CCA model. Microscopic images showed the proliferation of CCAO within the hydrogel, with the formation of classical balloon-like structures as well as denser and tightly packed morphologies (Fig. 6J). Conventional cultures of CCAOs in BME are absent of these dense, tightly packed morphologies (Fig. S15). Importantly, F-actin staining revealed the maintenance of clearly heterogeneous, patient-specific actin arrangements within the three organoid lines, showing its potential usefulness for personalized medicine applications (Fig. 6K). In all, this proof of concept utilizing decellularized CCA scaffolds for tumor tissue engineering resulted in the fabrication of a hydrogel that can be combined with cell culture as well as advanced organoid culture. Using native tumor-ECM derived hydrogels could provide a more complex and faithful representation of the in vivo extracellular environment.

3. Discussion

Extracellular matrix dysregulation is emerging as a crucial contributory mechanism in the development and progression of cancer [55,56]. However, detailed information on the composition and mechanics associated with this dysregulation is lacking, partly due to difficulties associated with capturing the complex compositions of extracellular matrix. One of the major goals of this study was to uncover the categorical constituents of human liver cancer extracellular matrices, at a biochemical and biomechanical level. This will potentially advance the biological understanding of the influence of the extracellular matrix on various facets of tumor behavior. Further advances in extracellular matrix characterization will provide better insights into the complex three-dimensional network of molecules that, in turn, will complement delineation of tumor initiation, progression, invasion, and metastasis processes.

Here we used Triton X-100 as a decellularization agent to decellularize biopsies of tumor and adjacent tumor-free liver tissue. Triton X-100 is, in contrast to more harsh agents such as sodium dodecyl sulphate, superior in retaining biologically relevant components and collagen fiber organization [22,57–59]. This, combined with a robust mass spectrometry workflow, allowed us to observe that the human liver cancer matrisome constitutes a large number of relatively lowly abundant proteins associated to the matrisome. These proteins are expected to mediate various processes in the assembly of ECM and thereby directly regulate tumor cell behavior. The method employed in this study identified numerous proteins - many of which in low abundances – which reassures the capability of this combined approach in delivering in-depth coverage of composition [60–62]. Our data furthermore suggests that the division of human liver (cancer) matrisome proteins, core and associated, sketches the picture of a more dynamic fraction of the matrisome, as exhibited by a large amount of affected associated-proteins in a tumor setting, and a stable core network of collagens less

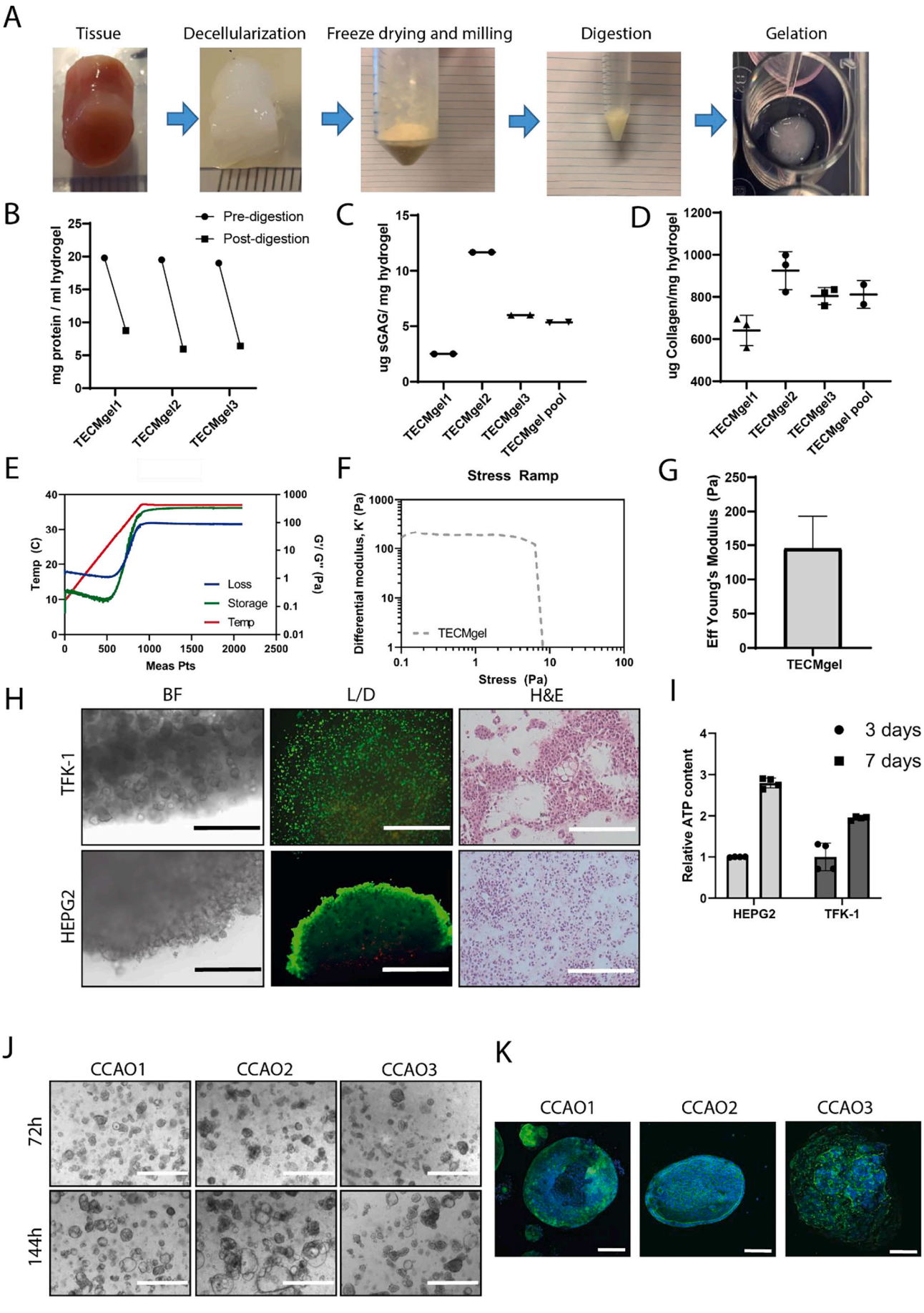

(caption on next page)

Fig. 6. Tumor ECM extracts can be employed to create a biocompatible tumor hydrogel.
A) The gelation preparation protocol consists of obtaining patient material, decellularization of the tissue, freeze-drying and subsequent milling into fine powder, digestion of powder in a pepsin solution, and neutralization to a physiological pH, salinity, and temperature to form a tumor ECM hydrogel (TECMgel).
B) Digestion efficiency of TECMgel (N = 3) by comparing the original protein input and the total output per ml after solubilization.
C) Quantification of sulfated glycosaminoglycan content for each separate batch (N = 3) and combined (termed 'TECMgel pool')
D) Quantification of collagen content for each separate batch (N = 3) and combined (termed 'TECMgel pool').
E) Oscillatory rheology shows the rheological behavior for storage and loss modulus of the TECMgel pool. After ramping temperature to 37 °C, gelation occurs to form an elastic material with $G' >> G''$.
F) Differential modulus as a function of shear stress measured in a stress ramp for TECMgel pool, showing abrupt rupture at a stress of ~10 Pa.
G) Nanoindentation measurements for different locations within one TECMgel pool highlights the local stiffness heterogeneity.
H) HEPG2 and TFK-1 culture in TECMgel pool displays the biocompatibility for both cell lines. BF = brightfield microscopy, L/D = Live/Dead staining using Calcein AM/Propium Iodide, H&E = Hematoxylin and Eosin. Scale bars for BF indicates 400 μm, for L/D 1000 μm, for H&E 400 μm.
I) Both HepG2 and TFK-1 display increased cell proliferation over time as determined by total ATP content.
J) Brightfield microscope pictures of patient-derived CCA organoids (N = 3) cultured in TECMgel pool. Scale bars indicate 1000 μm.
K) Confocal imaging of F-actin (green) and DAPI (blue) showing the different morphologies of the three patients and its retention in the TECMgel pool. Scale bars indicate 100 μm.

affected in regards to overall abundance. This is similar to recent data in liver fibrosis which also showed that alterations to liver matrisome proteins is much more diverse than solely the accumulation of collagen [63].

Simultaneously, this core network of collagens shows profound changes in architecture, associated with tumor-type dependent mechanical properties on a macro- and micro-scale. The physical properties of tumor ECM, such as stiffness and alignment, are of importance during various aspects of cancer progression [64]. Perturbed collagen architectures have been observed surrounding tumors, likely due to cellular remodeling of ECM to form regions of aligned collagen fibers, which in turn affects cell behavior in a reciprocal way [12,65]. Thus, characterizing the biomechanical properties of these scaffolds is important due to the mechanosensitivity of many cell types. Importantly, here we attempted to create multi-scale data to integrate local mechanical properties with larger macroscopic scales, which both play an important role in the hierarchical structure of healthy and diseased tissue. A difference is observed when comparing the extracellular matrix on different scales (i.e. nanoindentation compared to rheological measurements), with nanoindentation results exhibiting a higher stiffness overall, and showing more abundant differences when comparing tumor and adjacent decellularized matrices. It stands to reason that as the scale of testing gets closer to testing single ECM-components, e.g. individual collagen fibrils (diameter 150 nm [66]), so does the effective modulus converge toward the modulus of these individual components. A similar effect was seen in healthy liver tissue measurements [67]. Additionally, using a different sized tip in atomic force microscope (AFM) indentation testing resulted in a 100-fold change in modulus in articular cartilage, and this effect was absent in homogenous agarose gels [68]. This highlights the importance of measuring native-like tissue, consisting of a large complex ensemble of proteins, rather than aspects in isolation. This approach is complementary to the more traditional reductionist point of view on tumor tissue engineering, where specific collagen molecules and GAGs are isolated [69] to provide mechanistic insight at a molecular level not readily available through decellularization. Our comprehensive analysis of the intricate and complicated interactions that govern liver cancer extracellular matrix remodeling on a biochemical and biomechanical level can be used as a platform for more in-depth, mechanistic, investigations. Our findings illustrate that changes to the fundamental building blocks do not solely account for changes in mechanical properties, but also that other factors such as alignment and structure contribute significantly.

Furthermore, we developed a biocompatible, biomimetic ECM hydrogel from CCA tissue by combining decellularized CCA ECM and solubilization methods. Cytocompatibility was initially assessed with liver-cancer cell lines HepG2 and TFK-1, which both showed the formation of viable, proliferating, tumor-like dense structures. Subsequently, patient-derived organoids were used to create a complete patient-derived model. Recently, significant attention has been given to the development of ECM-derived hydrogels for organoids from a variety of different healthy organs [51,70,71]. By applying the same principle to tumors, more representative human disease models may be developed. We observed differing morphologies (balloon-like vs denser structures) within our hydrogel, which could be due to the high heterogeneity in stiffness observed within the hydrogel, particularly compared to BME. This builds upon previous research which showed organoid morphology and proliferation is dependent on hydrogel stiffness [48,72,73]. Whether the heterogeneity in morphology represents an increase in intratumoral heterogeneity recapitulation, which is critical for (personalized) drug response testing, remains to be elucidated [74–76]. The potential of tumor organoids for therapeutic testing in a personalized medicine setting is evident, although some outstanding questions remain, including whether the culture of organoids in an artificial, animal-derived environment (basement membrane extract-based hydrogels, with their associated limitations regarding animal-derivation, tumor mismatch, and lack of interstitial matrix-based components [77]) is sufficient to capture true patient responses. Thus, utilizing tumor-derived hydrogels could provide an alternative avenue, more representative of the human tumor extracellular environment, for developing personalized medicine applications.

The exact mechanisms by which the identified assembly of human liver matrisome influence biological processes remains unclear and should be subjected to further analysis. However, the experimental pipeline presented in this study provides the opportunity to produce human-derived extracellular matrix scaffolds that are thoroughly characterized by proteomics with respect to the distribution of matrisome proteins and biomechanically characterized on a macro- and micro-scale. The experimental setup presented in this study is applicable to any type of tissue and can be employed to gain better understanding of the complex compositions of the native human cancer matrisome and shed new light on its role in various physiological processes.

4. Conclusions

In this research, we utilized decellularization to increase our understanding of PLC extracellular matrix on a biochemical and biomechanical scale. The myriad of uncovered proteins in both a tumor and adjacent setting highlights the complexity of the human PLC matrisome and stresses the importance of considering the full ensemble of proteins in the development of liver cancer. Furthermore, the mechanical contribution of ECM within liver cancer on both a macro- and micro-scale provides integration of mechanics between scales and insight into the changes in stiffness during cancer development in the liver. Lastly, as a proof-of-concept this research shows the production of a tumor extracellular matrix-derived hydrogel able to sustain tumor organoids to create a patient-derived tumor model, providing an avenue for utilization in personalized medicine applications.

5. Methods

5.1. Tissue acquisition

HCC (N = 12) and CCA (N = 12, intrahepatic CCA N = 9, perihilar CCA N = 3) tissue samples and non-tumor adjacent samples were obtained from patients who underwent a curative-intent surgical resection or liver transplantation. Additional information on tumor and patient characteristics can be found in Supplementary Table 1. All surgical procedures were performed at the Erasmus MC in Rotterdam. Use of tissue for research purposes was approved by the Medical Ethical Council of the Erasmus MC and written informed consent was given by all patients (MEC-2013-143, MEC-2014-060). Samples were confirmed to be tumor or non-tumorous with histopathological assessment. All samples were initially stored at 4 °C in Belzer UW cold storage solution (UW, Bridge to Life) and processed at a later stage for decellularization.

5.2. Decellularization procedure

All tissues were washed with dH_20 to remove traces of blood or debris. Subsequently, tissue samples underwent three freeze-thaw cycles to disrupt cell membranes through formation of intra-cellular ice crystals. All tissue samples, regardless of origin or method of retrieval, were decellularized with a solution consisting of 4 % Triton-X-100 and 1 % NH_3 (hereafter referred to as TX-100 solution) and subsequent DNAse treatment. Tissue samples were placed in a beaker on a magnetic stirrer (1500 RPM) at room temperature (RT). TX-100 solution was replaced every 1 h for a total of 10 cycles, and a subsequent overnight (O/N) cycle, which resulted in the tissues obtaining a translucent, white appearance. TX-100 solution was washed out of the tissue samples with dH_2O for a minimum of 1 h. Lastly, tissues were incubated with DNAse solution (10 mg/ml DNase type I (Sigma) in 154 mM NaCl +100 mM $CaCl_2$ + 100 mM $MgCl_2$) for 3.5 h at 37 °C. Biopsy samples were taken before and after complete decellularization for the various analyses.

5.3. DNA quantification

DNA extraction from tumor and non-tumor adjacent tissue samples, before and after decellularization, was done using a QIAamp DNA Mini Kit (Qiagen) according to manufacturer's instructions. Subsequently, total DNA content was measured using a NanoDrop spectrophotometer (Thermo Fisher Scientific).

5.4. Collagen and sulfated glycosaminoglycan quantification

The total collagen content was measured using a total collagen kit (QuickZyme biosciences) according to manufacturer's protocol. Absorbance was measured at 570 nm using an infinite M nano plate reader (Tecan). Sulfated glycosaminoglycan (sGAG) was measured using a GAG assay kit (Biocolor) according to manufacturer's protocol. Samples were digested at 65 °C with Papain (10 mg/ml, Sigma) for 8 h. Absorbance was measured at 680 nm using a Model 680 XR Microplate Reader (Bio-Rad).

5.5. Proteomic sample preparation

100 μl 50 mM Tris-HCl (pH 8.0) was added to the decellularized ECM scaffolds and snap frozen in liquid nitrogen, followed by homogenizing using a dismembrator. The sample was heated in a thermomixer for 5 min at 95 °C. 90 μl 50 mM Tris-HCl and 5 μl 100 mM of 1,4-Dithiothreitol (DTT) were added and the sample was incubated at 50 °C for 60 min. Subsequently, 5 μl 200 mM of 2-Chloroacetamide (CAA) was added and the sample was incubated at RT for 30 min. Then, 100 μl 50 mM Tris-HCl and 10 μl PNGase F (500 units/ml) was added and the samples were further incubated at 37 °C for 4 h, followed by 5 min at 95 °C. Finally, 25 μl Sodium Deoxycholate (SDC) and trypsin was added (1100, trypsin: protein) and incubated in a thermomixer O/N at 30 °C and 1100 RPM. The next day, 25 μl 10 % trifluoroacetic acid (TFA) was added to the sample, followed by 2× washes with ethylacetate: 300 μl ethylacetate (H_2O saturated) was added, the mixture was mixed vigorously and then centrifuged for 2 min at 5000 rpm. The upper layer was removed, followed by 45 min in the speedvac to evaporate the solvent and reduce the sample volume. The protein digest was desalted using C18 stage tips. This was repeated for the flow through. The stage tip was then washed with 100 μl 0.1 % TFA, centrifuged for 10 min at 2000 rpm, followed by 2× elution of the peptides with 75 μl 50 % acetonitrile (AcN) and centrifugation for 8 min at 2000 rpm. Next, peptides were dried in the speedvac and reconstituted in 25 μl 2 % AcN, 0.5 % formic acid (FA). Nanoflow liquid chromatography tandem mass spectrometry (nLC-MS/MS) was performed on an EASY-nLC coupled to an Orbitrap Fusion Lumos Tribrid mass spectrometer (Thermo), operating in positive mode. Peptides were separated on a ReproSil-C18 reversed-phase column (Dr Maisch; 15 cm × 50 μm) using a linear gradient of 0–80 % acetonitrile (in 0.1 % formic acid) during 90 min at a rate of 200 nl/min. The elution was directly sprayed into the electrospray ionization (ESI) source of the mass spectrometer. Spectra were acquired in continuum mode; fragmentation of the peptides was performed in data-dependent mode by HCD.

5.6. Proteomic data processing

Raw mass spectrometry data were analyzed using the Proteome Discoverer 2.3 software suite (ThermoFisher Scientific). The Mascot search algorithm (version 2.3.2, MatrixScience) was used for searching against the Uniprot database (taxonomy: *Homo sapiens*). The peptide tolerance was typically set to 10 ppm and the fragment ion tolerance was set to 0.8 Da. A maximum number of 2 missed cleavages by trypsin were allowed and carbamidomethylated cysteine and oxidized methionine were set as fixed and variable modifications, respectively. Typical contaminants were omitted from the output tables.

5.7. Proteomic data analysis

To identify and categorize the detected proteins that are related to the extracellular matrix, the dataset was compared to and filtered with the MatrisomeDB database [30]. MatrisomeDB uses domain-based organization of matrisome-related proteins to obtain a complete collection of ECM proteomic data. Proteins identified are subdivided into ECM-affiliated proteins, secreted factors, collagens, ECM regulators, ECM glycoproteins, and proteoglycans. The identified matrisome proteins were further classified into 3 categories: a core ensemble of proteins, differentially expressed (DE) proteins, and exclusive proteins. The core ensemble of proteins consist of proteins that are present in all replicates of all conditions. Proteins are differentially expressed if the adjusted p-val is >0.05. Proteins are identified as 'exclusive' if they are present in samples of one condition, while absent in all replicates of another condition. To note, the difference between DE proteins and exclusive proteins is likely due to the sensitivity of mass spectrometry. Therefore, DE proteins and exclusive proteins were combined to apply enrichment analysis using the fgsea (version 1.16.0) R package. To compare the proteomic data to global RNA expression, the TCGA data portal was used to determine DE genes between two conditions (CCA vs CCA-ADJ (N = 36 cancer samples, N = 9 normal samples) and HCC vs HCC-ADJ (N = 373 cancer samples, N = 50 normal samples)) as previously described [78]. Benjami and Hochberg (BH) method was used to calculate the False Discovery Rate (FDR). For the comparison between CCA and HCC, gene expression profiles were obtained from the GEO database (GSE15765) which contained both CCA and HCC samples (CCA N = 13, HCC N = 70). DE genes were obtained by using the GEO2R online tool (www.ncbi.nlm.nih.gov/geo/geo2r/) [79].

5.8. Histological and immunohistochemical staining

HCC, CCA, and non-tumor adjacent samples before and after decellularization were fixed in 4 % paraformaldehyde (PFA, Fresenius Kabi). The samples were subsequently embedded in paraffin, cut into 4 μm sections and processed for routine histomorphological stains: Hematoxylin-Eosin (H&E), PicroSirius Red (PSR), Gomori's silver impregnation (GOM), and 4′,6-diamidino-2-phenylindole (DAPI, Vectashield, Vectorlabs). Stained slides were imaged with a Zeiss Axioskop 20 microscope and captured with a Nikon DS-U1 camera, with the exception of DAPI which was analyzed using EVOS microscope (Thermofisher).

5.9. Second Harmonic Generation imaging and analysis

To visualize collagen bundles, Second Harmonic Generation (SHG) was used [80]. In short, a Leica water dipping lens (20×) with numerical aperture of 1.00 was used to deliver the excitation signal and to collect the emission signal. The fluorescence of collagen was collected using 880 nm excitation. Averaging was performed over 4 lines for SHG to reduce the effect of background noise. Total Collagen fibers were identified from SHG images of the decellularized ECM scaffolds using the ctFIRE software package (http://loci.wisc.edu/software/ctFIRE, v.2.0b). Further analysis of fiber to fiber orientation was completed using the CurveAlign software package (http://loci.wisc.edu/software/curvealign, v.4.0b). For each sample (N = 3 per condition), at least 2 non overlapping microscopic fields at 20× were acquired and analyzed with the software packages.

5.10. Hydrogel preparation procedure

Tumor ECM hydrogel (TECMgel) was prepared from CCA decellularized scaffolds (N = 3 patients) by cutting the ECM into thin discs (200 μm thickness) using a cryotome (Leica) at −15 °C. TECMgel was created according to our previously published protocol [51]. The decellularized ECM was frozen at −20 °C and freeze-dried using a lyophilizer (Zirbus Technology Sublimator 400) for 72 h. The freeze-dried decellularized ECM was pulverized using a Retsch ZM200 knife mill with a <250 μm sieve.

The obtained powder was digested over a period of 72 h at RT with a concentration of 40 mg/ml in 10 % (w/w) pepsin (3200–4500 U/mg, Sigma) in 0.5 M Acetic Acid. Next, 5 M NaOH, 10 % (v/v) 10× PBS, and 10 % (v/v) Advanced DMEM was added while the mixture was cooled on ice. The pH was adjusted to be between 7.4 and 7.6 with 1 M NaOH or 1 M HCL. Small aliquots were taken to confirm the desired pH with an electronic pH meter (VWR symphony SB70P). The obtained solutions were spun down at 1811 g for 30 min at 4 °C in order to remove undigested debris. 25 μl droplets of the pre-gel solution were placed in a well-plate and incubated for 30 min at 37 °C for 60 min. After confirmation of gelation of the droplets, the remained of the pre-gel solutions were pooled and stored at 6 mg/ml concentration at −20 °C.

5.11. Rheology

A rotational rheometer (MCR 501; Anton Paar, Graz, Austria) with a stainless steel parallel plate geometry with a diameter of 20 mm was used in oscillatory mode to determine the storage (G′) and loss (G″) moduli. Both decellularized scaffolds and hydrogel samples were measured. For the decellularized scaffolds, scaffolds were placed on the bottom plate, after which the top plate was lowered to a gap height of 0.5 mm. First, the surface contact point was determined through a linear compressive ramp from a gap of 0.5 mm to a gap of 0.1 mm with the normal stress measured every 5 s and 0.1 mm/20 points decrease, which was stopped upon 5 subsequent increases in normal force (N), signifying that contact was made with the scaffold. Next, a linear oscillatory shear test was performed (shear strain amplitude of 0.5 %, oscillation frequency 0.5 Hz) to measure the storage and loss shear moduli. The sample was then compressed to 10 % compressive strain and the time-dependent response of the normal force was measured for a fixed duration while again measuring storage and loss moduli to obtain the steady-state normal stress. In total, the sample was compressed 5 times in steps of 10 % compressive strain, measuring the material properties at each compression step. Analysis of normal stress and shear storage modulus data was performed through fitting a single-exponential decay model to the data obtained. The data was corrected for the size of each sample and increase in size after each compression step (i.e., at 30 % compression the nominal stress values were corrected by dividing by 1/(1-0.3), the storage modulus values at this compression level were divided by 1/(1-0.3)^2). An estimate of the Young's modulus (E) was determined over the whole range of compressive strains by fitting a linear curve to the values obtained at each compressive strain (0, 10, 20, 30, 40, 50 % compression). See Supplemental Fig. 8 for additional information on protocol and analysis method. For the hydrogel samples (both TECMgel and BME), cooled pre-gel samples (50 μl) were pipetted on the bottom plate, which was cooled to 10 °C. The test geometry was lowered to a gap height of 1 mm and excess hydrogel was discarded. The temperature was increased to 37 °C at a rate of 1 degree every 30 s, with measurements taken every second to determine gelation. Subsequently, frequency sweeps (f: 0.01–10 Hz, Slope: 10 pt./decade) and shear stress ramps were performed by increasing the shear stress from 0.01 Pa to 1000 Pa with 10 points per decade. Each point was taken after 5 s of applied stress to allow the sample to reach a steady state. Lastly, the recovery of the material after being subject to high stress was measured with a single frequency oscillation (1 Hz) at a shear strain amplitude of 0.5 %. The recovery was monitored by measuring one point every 5 s over the course of 15 min.

5.12. Nanoindentation measurements and analysis

The effective Young's modulus was measured using a Chiaro Nanoindenter (Optics11 Life). For hydrogel measurements, 200 μl of cold pre-gel droplets were pipetted into 35 mm petri dishes and allowed to solidify at 37 °C for 1 h. For decellularized tissue, scaffolds were glued inside a 35 mm petri dish using NOA61 (Norland). The probe used had a stiffness of 0.027 N/m and a spherical tip with a radius of 3 μm. Measurements were performed submerged in PBS. Indentations were made with a loading rate of 2 μm/s. The effective Young's modulus was calculated using the Hertzian contact model by the Optics 11 Life data viewer software (version 2) [81]. Indentations for each sample were performed at locations separated by 100 μm in 3 × 3 and 10 × 10 square matrices for hydrogels and scaffolds respectively. Measurements without a distinct contact point or with an otherwise unreliable model fit (<0.9 R^2) were regarded as outliers and discarded from further analysis.

5.13. Cell culture

HEPG2 cells were cultured in DMEM (Gibco) supplemented with 10 % fetal calf serum (FCS, Sigma) and 1 % (100 U/ml) penicillin/streptomycin (PS, Gibco). TFK-1 cells were cultured in RPMI 1640 supplemented with 10 % FCS and 1 % PS. HEPG2 cells were split approximately every 3–6 days 1:2–1:4 using trypsin, TFK-1 cells were split approximately every 3–5 days 1:3-:1:5. For experiments, cells were mixed with TECMgel or basement membrane extract (BME) at a concentration of 100,000 cells/well in a 24-well plate.

5.14. Organoid culture

Organoid initiation was performed as previously described [4]. In short, biopsies were minced and digested in 2.5 mg/ml collagenase type A (Sigma) for 30–120 min at 37 °C. The duration of digestion depended on the amount of desmoplasia and/or fibrosis present in the biopsy. Digestion was continued until no visible pieces of tissue remained.

Subsequently, the cell suspension was strained (100 μm cell strainer) and washed in cold Advanced DMEM. After centrifugation (453*g*, 5 min, 4 °C), the cell pellet was suspended in basement membrane extract (BME, Cultrex). The mixture of cells and BME was plated in droplets in 24- or 48-well suspension culture plates (Greiner). BME was allowed to solidify at 37 °C for 30–45 min before addition of startup medium (SEM, Table S2). Medium was refreshed every 3 to 4 days. After the first passaging, SEM was replaced by expansion medium (EM, Table S3). Organoids were passaged in 1:3 to 1:6 ratios approximately every 7 days depending on their rate of proliferation. Passaging was done with mechanical dissociation of organoid fragments and BME and subsequent replating of organoid fragments in TECMgel or BME.

5.15. Live/dead staining

Samples were incubated in the corresponding medium for each cell line supplemented with 100 μg/ml Hoechst 33342, 12.5 μg/ml propidium iodide (PI, Sigma-Aldrich), 1 μM calcein acetoxymethyl ester (Calcein AM, Thermo Fisher Scientific) for 30 min at 37 °C in the dark. Images were captured with an EVOS fluorescent microscope.

5.16. Immunocytochemical staining

To evaluate localization of actin filaments, immunofluorescent staining was performed combined with whole mount confocal microscopy. All samples were fixed for 20 min using 4 % PFA and permeabilized with 0.1 % Triton X-100 diluted in PBS for 30 min. Subsequently, samples were exposed to 5 % BSA diluted in PBS to prevent nonspecific antibody binding. Cytoskeletal staining with Phalloidin Alexa Fluor™ 488 (4:200, Fisher Scientific) was incubator for 1 h and nuclear staining with DAPI was incubated for 30 min at RT before imaging with a Leica 20× (NA 1.0) water dipping lens on a Leica DM6000 CFS microscope with a LEICA TCS SP5 II confocal system.

5.17. Cell proliferation measurements

Cell viability was measured using CellTiter-Glo (Promega) according to manufacturer's instructions.

5.18. Statistical analysis

All statistical analyses were conducted using GraphPad Prism (version 8, GraphPad Software) or R (version 4.0.3, R Core Team). Qualitative data were analyzed with the χ^2 or Fisher exacts tests and were presented with numbers and percentages. Continuous variables were tested using a Mann-Whitney-*U* test and presented graphically as means with standard deviation or standard error of mean. Multi-variate analysis was done with 2-way ANOVA with multiple comparison testing for different time points and Bonferroni correction. If alternative statistical analysis was used, a description of the method and test results was noted. In all tests, a p value of <0.05 is considered significant.

Ethics approval

Use of tissue for research purposes was approved by the Medical Ethical Council of the Erasmus MC (MEC-2014-060 and MEC-2013-143) and written informed consent was given by all patients.

Funding

This project was partly funded by the Erasmus MC Human Disease Model Award 2018 (HDMA-380801), by the Medical Delta program grant (Regenerative Medicine 4D), by ENW-XS (Project OCENW.XS21.2.003) of the Dutch Research Council (NWO), by the Convergence program Syn-Cells for Health(care) under the theme of Health and Technology, and a grant from the NWO Talent Program (VI.C.182.004).

CRediT authorship contribution statement

GST, MMAV designed the study. MMAV, LJWL and GHK obtained funding. GST, MD aided in the collection of tissues. GST, JW optimized decellularization of primary liver cancer tissue. GST, JT, IM, and JC performed characterization and analysis of the decellularized scaffolds. GST, KM cultured organoids. GST, JT, JD aided in the conception and implementation of mass spectrometry experiments, and JT and GST performed the analysis. GST, JC, IM, GHK set-up mechanical characterization of decellularized scaffolds, with GST and IM conducting rheological measurements and JC conducting nanoindentation measurements. GST, IM, IS, JC performed data analysis of mechanical measurements. GST, JW performed solublization and characterization of the hydrogel. GST collected all data and drafted the figures. GST, LJWL, MMAV wrote the manuscript. All authors critically reviewed and revised the manuscript.

Declaration of competing interest

Authors declare that they have no competing interests.

Data availability

MS data can be found at PXD035261.

Acknowledgements

N/A.

Appendix A. Supplementary data

Supplementary data to this article can be found online at https://doi.org/10.1016/j.bioadv.2023.213289.

References

[1] T.R. Cox, J.T. Erler, Fibrosis and cancer: partners in crime or opposing forces? Trends Cancer 2 (6) (2016) 279–282.
[2] A. Ray, P.P. Provenzano, Aligned forces: origins and mechanisms of cancer dissemination guided by extracellular matrix architecture, Curr. Opin. Cell Biol. 72 (2021) 63–71.
[3] C. Jensen, D.H. Madsen, M. Hansen, H. Schmidt, I.M. Svane, M.A. Karsdal, N. Willumsen, Non-invasive biomarkers derived from the extracellular matrix associate with response to immune checkpoint blockade (anti-CTLA-4) in metastatic melanoma patients, J. Immunother. Cancer 6 (1) (2018) 1–10.
[4] S.H. Nielsen, A.J. Mouton, K.Y. DeLeon-Pennell, F. Genovese, M. Karsdal, M. L. Lindsey, Understanding cardiac extracellular matrix remodeling to develop biomarkers of myocardial infarction outcomes, Matrix Biol. 75 (2019) 43–57.
[5] E. Brauchle, J. Kasper, R. Daum, N. Schierbaum, C. Falch, A. Kirschniak, T. E. Schaeffer, K. Schenke-Layland, Biomechanical and biomolecular characterization of extracellular matrix structures in human colon carcinomas, Matrix Biol. 68 (2018) 180–193.
[6] G.R. Liguori, T.T.A. Liguori, S.R. de Moraes, V. Sinkunas, V. Terlizzi, J.A. van Dongen, P.K. Sharma, L.F.P. Moreira, M.C. Harmsen, Molecular and biomechanical clues from cardiac tissue decellularized extracellular matrix drive stromal cell plasticity, Front. Bioeng. Biotechnol. 8 (2020) 520.
[7] M. Urbanczyk, S.L. Layland, K. Schenke-Layland, The role of extracellular matrix in biomechanics and its impact on bioengineering of cells and 3D tissues, Matrix Biol. 85 (2020) 1–14.
[8] A. Naba, K.R. Clauser, H. Ding, C.A. Whittaker, S.A. Carr, R.O. Hynes, The extracellular matrix: tools and insights for the "omics" era, Matrix Biol. 49 (2016) 10–24.
[9] I.N. Taha, A. Naba, Exploring the extracellular matrix in health and disease using proteomics, Essays Biochem. 63 (3) (2019) 417–432.
[10] E.C. Filipe, J.L. Chitty, T.R. Cox, Charting the unexplored extracellular matrix in cancer, Int. J. Exp. Pathol. 99 (2) (2018) 58–76.
[11] M.O. Riener, F.R. Fritzsche, C. Soll, B.C. Pestalozzi, N. Probst-Hensch, P.A. Clavien, W. Jochum, A. Soltermann, H. Moch, G. Kristiansen, Expression of the extracellular matrix protein periostin in liver tumours and bile duct carcinomas, Histopathology 56 (5) (2010) 600–606.
[12] G.S. van Tienderen, B. Groot Koerkamp, J.N.M. Ijzermans, L.J.W. van der Laan, M. Verstegen, Recreating tumour complexity in a dish: organoid models to study liver cancer cells and their extracellular environment, Cancers (Basel) 11 (11) (2019) 1706.

[13] T. Luedde, R.F. Schwabe, NF-κB in the liver—linking injury, fibrosis and hepatocellular carcinoma, Nat. Rev. Gastroenterol. Hepatol. 8 (2) (2011) 108.
[14] A.E. Sirica, G.J. Gores, Desmoplastic stroma and cholangiocarcinoma: clinical implications and therapeutic targeting, Hepatology 59 (6) (2014) 2397–2402.
[15] J.U. Marquardt, J.B. Andersen, S.S. Thorgeirsson, Functional and genetic deconstruction of the cellular origin in liver cancer, Nat. Rev. Cancer 15 (11) (2015) 653.
[16] N. Razumilava, G.J. Gores, Classification, diagnosis, and management of cholangiocarcinoma, Clin. Gastroenterol. Hepatol. 11 (1) (2013) 13–21, e1.
[17] P.C. Valery, M. Laversanne, P.J. Clark, J.L. Petrick, K.A. McGlynn, F. Bray, Projections of primary liver cancer to 2030 in 30 countries worldwide, Hepatology 67 (2) (2018) 600–611.
[18] H. Sung, J. Ferlay, R.L. Siegel, M. Laversanne, I. Soerjomataram, A. Jemal, F. Bray, Global cancer statistics 2020: GLOBOCAN estimates of incidence and mortality worldwide for 36 cancers in 185 countries, CA Cancer J. Clin. 71 (3) (2021) 209–249.
[19] P.M. Crapo, T.W. Gilbert, S.F. Badylak, An overview of tissue and whole organ decellularization processes, Biomaterials 32 (12) (2011) 3233–3243.
[20] T.W. Gilbert, T.L. Sellaro, S.F. Badylak, Decellularization of tissues and organs, Biomaterials 27 (19) (2006) 3675–3683.
[21] G. Mazza, W. Al-Akkad, A. Telese, L. Longato, L. Urbani, B. Robinson, A. Hall, K. Kong, L. Frenguelli, G. Marrone, Rapid production of human liver scaffolds for functional tissue engineering by high shear stress oscillation-decellularization, Sci. Rep. 7 (1) (2017) 5534.
[22] J. Willemse, M.M.A. Verstegen, A. Vermeulen, I.J. Schurink, H.P. Roest, L.J.W. van der Laan, J. de Jonge, Fast, robust and effective decellularization of whole human livers using mild detergents and pressure controlled perfusion, Mater. Sci. Eng. C 108 (2020), 110200.
[23] J. Willemse, F.J.M. Roos, I.J. Voogt, I.J. Schurink, M. Bijvelds, H.R. de Jonge, L.J. W. van der Laan, J. de Jonge, M.M.A. Verstegen, Scaffolds obtained from decellularized human extrahepatic bile ducts support organoids to establish functional biliary tissue in a dish, Biotechnol. Bioeng. 118 (2) (2021) 836–851.
[24] K.H. Hillebrandt, H. Everwien, N. Haep, E. Keshi, J. Pratschke, I.M. Sauer, Strategies based on organ decellularization and recellularization, Transpl. Int. 32 (6) (2019) 571–585.
[25] A. Daneshgar, O. Klein, G. Nebrich, M. Weinhart, P. Tang, A. Arnold, I. Ullah, J. Pohl, S. Moosburner, N. Raschzok, The human liver matrisome–Proteomic analysis of native and fibrotic human liver extracellular matrices for organ engineering approaches, Biomaterials 257 (2020), 120247.
[26] J. Wei, M. Hu, K. Huang, S. Lin, H. Du, Roles of proteoglycans and glycosaminoglycans in cancer development and progression, Int. J. Mol. Sci. 21 (17) (2020) 5983.
[27] S. Morla, Glycosaminoglycans and glycosaminoglycan mimetics in cancer and inflammation, Int. J. Mol. Sci. 20 (8) (2019) 1963.
[28] G. Tóth, D. Pál, S. Sugár, I. Kovalszky, K. Dezső, G. Schlosser, L. Drahos, L. Turiák, Expression of glycosaminoglycans in cirrhotic liver and hepatocellular carcinoma—a pilot study including etiology, Anal. Bioanal. Chem. (2022) 1–10.
[29] H. Lv, G. Yu, L. Sun, Z. Zhang, X. Zhao, W. Chai, Elevate level of glycosaminoglycans and altered sulfation pattern of chondroitin sulfate are associated with differentiation status and histological type of human primary hepatic carcinoma, Oncology 72 (5–6) (2007) 347–356.
[30] X. Shao, I.N. Taha, K.R. Clauser, Y. Gao, A. Naba, MatrisomeDB: the ECM-protein knowledge database, Nucleic Acids Res. 48 (D1) (2020) D1136–D1144.
[31] M. Uhlén, L. Fagerberg, B.M. Hallström, C. Lindskog, P. Oksvold, A. Mardinoglu, Å. Sivertsson, C. Kampf, E. Sjöstedt, A. Asplund, Tissue-based map of the human proteome, Science 347 (6220) (2015), 1260419.
[32] A.D. Bradshaw, Diverse biological functions of the SPARC family of proteins, Int. J. Biochem. Cell Biol. 44 (3) (2012) 480–488.
[33] Z.C. Nwosu, D.A. Megger, S. Hammad, B. Sitek, S. Roessler, M.P. Ebert, C. Meyer, S. Dooley, Identification of the consistently altered metabolic targets in human hepatocellular carcinoma, Cell. Mol. Gastroenterol. Hepatol. 4 (2) (2017) 303–323, e1.
[34] C. Zhang, Y. Liang, M.-H. Ma, K.-Z. Wu, D.-Q. Dai, KRT15, INHBA, MATN3, and AGT are aberrantly methylated and differentially expressed in gastric cancer and associated with prognosis, Pathol. Res. Pract. 215 (5) (2019) 893–899.
[35] E.C. Chen, T.A. Karl, T. Kalisky, S.K. Gupta, C.A. O'Brien, T.A. Longacre, M. van de Rijn, S.R. Quake, M.F. Clarke, M.E. Rothenberg, KIT signaling promotes growth of colon xenograft tumors in mice and is up-regulated in a subset of human colon cancers, Gastroenterology 149 (3) (2015) 705–717, e2.
[36] P. Ulivi, L. Mercatali, G.-L. Casoni, E. Scarpi, L. Bucchi, R. Silvestrini, S. Sanna, M. Monteverde, D. Amadori, V. Poletti, Multiple marker detection in peripheral blood for NSCLC diagnosis, PLoS One 8 (2) (2013), e57401.
[37] K. Shi, N. Li, M. Yang, W. Li, Identification of key genes and pathways in female lung cancer patients who never smoked by a bioinformatics analysis, J. Cancer 10 (1) (2019) 51.
[38] A. Mesci, F. Lucien, X. Huang, E.H. Wang, D. Shin, M. Meringer, C. Hoey, J. Ray, P. C. Boutros, H.S. Leong, RSPO3 is a prognostic biomarker and mediator of invasiveness in prostate cancer, J. Transl. Med. 17 (1) (2019) 1–11.
[39] J. Harb, P.-J. Lin, J. Hao, Recent development of wnt signaling pathway inhibitors for cancer therapeutics, Curr. Oncol. Rep. 21 (2) (2019) 1–9.
[40] A. Klaus, W. Birchmeier, Wnt signalling and its impact on development and cancer, Nat. Rev. Cancer 8 (5) (2008) 387–398.
[41] A. Lucas, J.R. Yaron, L. Zhang, S. Ambadapadi, Overview of serpins and their roles in biological systems, Serpins (2018) 1–7.
[42] S.M. Zunder, H. Gelderblom, R.A. Tollenaar, W.E. Mesker, The significance of stromal collagen organization in cancer tissue: an in-depth discussion of literature, Crit. Rev. Oncol. Hematol. 151 (2020), 102907.
[43] P.P. Provenzano, K.W. Eliceiri, J.M. Campbell, D.R. Inman, J.G. White, P.J. Keely, Collagen reorganization at the tumor-stromal interface facilitates local invasion, BMC Med. 4 (1) (2006) 1–15.
[44] P.P. Provenzano, D.R. Inman, K.W. Eliceiri, J.G. Knittel, L. Yan, C.T. Rueden, J. G. White, P.J. Keely, Collagen density promotes mammary tumor initiation and progression, BMC Med. 6 (1) (2008) 1–15.
[45] Y. Liu, A. Keikhosravi, G.S. Mehta, C.R. Drifka, K.W. Eliceiri, Methods for quantifying fibrillar collagen alignment, in: Fibrosis, Springer, 2017, pp. 429–451.
[46] J.S. Bredfeldt, Y. Liu, C.A. Pehlke, M.W. Conklin, J.M. Szulczewski, D.R. Inman, P. J. Keely, R.D. Nowak, T.R. Mackie, K.W. Eliceiri, Computational segmentation of collagen fibers from second-harmonic generation images of breast cancer, J. Biomed. Opt. 19 (1) (2014), 016007.
[47] S.K. Venkatesh, M. Yin, J.F. Glockner, N. Takahashi, P.A. Araoz, J.A. Talwalkar, R. L. Ehman, Magnetic resonance elastography of liver tumors-preliminary results, AJR Am. J. Roentgenol. 190 (6) (2008) 1534.
[48] N. Gjorevski, N. Sachs, A. Manfrin, S. Giger, M.E. Bragina, P. Ordóñez-Morán, H. Clevers, M.P. Lutolf, Designer matrices for intestinal stem cell and organoid culture, Nature 539 (7630) (2016) 560.
[49] M. Ehrbar, A. Sala, P. Lienemann, A. Ranga, K. Mosiewicz, A. Bittermann, S. C. Rizzi, F.E. Weber, M.P. Lutolf, Elucidating the role of matrix stiffness in 3D cell migration and remodeling, Biophys. J. 100 (2) (2011) 284–293.
[50] A. Pathak, S. Kumar, Independent regulation of tumor cell migration by matrix stiffness and confinement, Proc. Natl. Acad. Sci. 109 (26) (2012) 10334–10339.
[51] J. Willemse, G. van Tienderen, E. van Hengel, I. Schurink, D. van der Ven, Y. Kan, P. de Ruiter, O. Rosmark, K. Schneeberger, B. van der Eerden, Hydrogels derived from decellularized liver tissue support the growth and differentiation of cholangiocyte organoids, Biomaterials 284 (2022), 121473.
[52] K.A. Jansen, A.J. Licup, A. Sharma, R. Rens, F.C. MacKintosh, G.H. Koenderink, The role of network architecture in collagen mechanics, Biophys. J. 114 (11) (2018) 2665–2678.
[53] D. Jiao, Z. Cai, S. Choksi, D. Ma, M. Choe, H.J. Kwon, J.Y. Baik, B.G. Rowan, C. Liu, Z.G. Liu, Necroptosis of tumor cells leads to tumor necrosis and promotes tumor metastasis, Cell Res. 28 (8) (2018) 868–870.
[54] L. Broutier, G. Mastrogiovanni, M.M.A. Verstegen, H.E. Francies, L.M. Gavarró, C. R. Bradshaw, G.E. Allen, R. Arnes-Benito, O. Sidorova, M.P. Gaspersz, Human primary liver cancer–derived organoid cultures for disease modeling and drug screening, Nat. Med. 23 (12) (2017) 1424.
[55] C. Walker, E. Mojares, A. del Río Hernández, Role of extracellular matrix in development and cancer progression, Int. J. Mol. Sci. 19 (10) (2018) 3028.
[56] M.W. Pickup, J.K. Mouw, V.M. Weaver, The extracellular matrix modulates the hallmarks of cancer, EMBO Rep. 15 (12) (2014) 1243–1253.
[57] L.J. White, A.J. Taylor, D.M. Faulk, T.J. Keane, L.T. Saldin, J.E. Reing, I. T. Swinehart, N.J. Turner, B.D. Ratner, S.F. Badylak, The impact of detergents on the tissue decellularization process: a ToF-SIMS study, Acta Biomater. 50 (2017) 207–219.
[58] H. Ren, X. Shi, L. Tao, J. Xiao, B. Han, Y. Zhang, X. Yuan, Y. Ding, Evaluation of two decellularization methods in the development of a whole-organ decellularized rat liver scaffold, Liver Int. 33 (3) (2013) 448–458.
[59] D.M. Faulk, C.A. Carruthers, H.J. Warner, C.R. Kramer, J.E. Reing, L. Zhang, A. D'Amore, S.F. Badylak, The effect of detergents on the basement membrane complex of a biologic scaffold material, Acta Biomater. 10 (1) (2014) 183–193.
[60] M.C. McCabe, L.R. Schmitt, R.C. Hill, M. Dzieciatkowska, M. Maslanka, W. F. Daamen, T.H. van Kuppevelt, D.J. Hof, K.C. Hansen, Evaluation and refinement of sample preparation methods for extracellular matrix proteome coverage, Mol. Cell. Proteomics 20 (2021).
[61] A.S. Barrett, M.J. Wither, R.C. Hill, M. Dzieciatkowska, A. D'Alessandro, J.A. Reisz, K.C. Hansen, Hydroxylamine chemical digestion for insoluble extracellular matrix characterization, J. Proteome Res. 16 (11) (2017) 4177–4184.
[62] S. Ernst, R. Langer, C.L. Cooney, R. Sasisekharan, Enzymatic degradation of glycosaminoglycans, Crit. Rev. Biochem. Mol. Biol. 30 (5) (1995) 387–444.
[63] G.E. Arteel, A. Naba, The liver matrisome–looking beyond collagens, JHEP Rep. 2 (4) (2020), 100115.
[64] S. Kumar, V.M. Weaver, Mechanics, malignancy, and metastasis: the force journey of a tumor cell, Cancer Metastasis Rev. 28 (1) (2009) 113–127.
[65] M.W. Conklin, J.C. Eickhoff, K.M. Riching, C.A. Pehlke, K.W. Eliceiri, P. P. Provenzano, A. Friedl, P.J. Keely, Aligned collagen is a prognostic signature for survival in human breast carcinoma, Am. J. Pathol. 178 (3) (2011) 1221–1232.
[66] E.D. Hay, Cell Biology of Extracellular Matrix, Springer Science & Business Media, 1991.
[67] D.W. Evans, E.C. Moran, P.M. Baptista, S. Soker, J.L. Sparks, Scale-dependent mechanical properties of native and decellularized liver tissue, Biomech. Model. Mechanobiol. 12 (3) (2013) 569–580.
[68] M. Stolz, R. Raiteri, A.U. Daniels, M.R. VanLandingham, W. Baschong, U. Aebi, Dynamic elastic modulus of porcine articular cartilage determined at two different levels of tissue organization by indentation-type atomic force microscopy, Biophys. J. 86 (5) (2004) 3269–3283.
[69] H. Bi, K. Ye, S. Jin, Proteomic analysis of decellularized pancreatic matrix identifies collagen V as a critical regulator for islet organogenesis from human pluripotent stem cells, Biomaterials 233 (2020), 119673.
[70] G.G. Giobbe, C. Crowley, C. Luni, S. Campinoti, M. Khedr, K. Kretzschmar, M.M. De Santis, E. Zambaiti, F. Michielin, L. Meran, Extracellular matrix hydrogel derived from decellularized tissues enables endodermal organoid culture, Nat. Commun. 10 (1) (2019) 1–14.

[71] S. Kim, S. Min, Y.S. Choi, S.-H. Jo, J.H. Jung, K. Han, J. Kim, S. An, Y.W. Ji, Y.-G. Kim, Tissue extracellular matrix hydrogels as alternatives to matrigel for culturing gastrointestinal organoids, Nat. Commun. 13 (1) (2022) 1–21.
[72] D.R. Hunt, K.C. Klett, S. Mascharak, H. Wang, D. Gong, J. Lou, X. Li, P.C. Cai, R. A. Suhar, J.Y. Co, Engineered matrices enable the culture of human patient-derived intestinal organoids, Adv. Sci. 8 (10) (2021), 2004705.
[73] E.A. Hushka, F.M. Yavitt, T.E. Brown, P.J. Dempsey, K.S. Anseth, Relaxation of extracellular matrix forces directs crypt formation and architecture in intestinal organoids, Adv. Healthc. Mater. 9 (8) (2020), 1901214.
[74] W. Shin, A. Wu, S. Min, Y.C. Shin, R.Y.D. Fleming, S.G. Eckhardt, H.J. Kim, Spatiotemporal gradient and instability of wnt induce heterogeneous growth and differentiation of human intestinal organoids, Iscience 23 (8) (2020), 101372.
[75] L. Li, H. Knutsdottir, K. Hui, M.J. Weiss, J. He, B. Philosophe, A.M. Cameron, C. L. Wolfgang, T.M. Pawlik, G. Ghiaur, Human primary liver cancer organoids reveal intratumor and interpatient drug response heterogeneity, JCI Insight 4 (2) (2019).
[76] Y. Zhao, Z.X. Li, Y.J. Zhu, J. Fu, X.F. Zhao, Y.N. Zhang, S. Wang, J.M. Wu, K. T. Wang, R. Wu, Single-cell transcriptome analysis uncovers intratumoral heterogeneity and underlying mechanisms for drug resistance in hepatobiliary tumor organoids, Adv. Sci. 8 (11) (2021), 2003897.
[77] C.S. Hughes, L.M. Postovit, G.A. Lajoie, Matrigel: a complex protein mixture required for optimal growth of cell culture, Proteomics 10 (9) (2010) 1886–1890.
[78] M. Li, Q. Sun, X. Wang, Transcriptional landscape of human cancers, Oncotarget 8 (21) (2017) 34534.
[79] R. Edgar, T. Barrett, NCBI GEO standards and services for microarray data, Nat. Biotechnol. 24 (12) (2006) 1471–1472.
[80] X. Chen, O. Nadiarynkh, S. Plotnikov, P.J. Campagnola, Second harmonic generation microscopy for quantitative analysis of collagen fibrillar structure, Nat. Protoc. 7 (4) (2012) 654–669.
[81] J.S. Field, M.V. Swain, Determining the mechanical properties of small volumes of material from submicrometer spherical indentations, J. Mater. Res. 10 (1) (1995) 101–112.